Journal of South American Earth Sciences 163 (2025) 105588

Contents lists available at ScienceDirect

Journal of South American Earth Sciences

journal homepage: www.elsevier.com/locate/jsames

Deformation of the Ecuadorian Inter-Andean valley and surroundings from a combined InSAR-GNSS velocity field 2017–2023.

Pedro Alejandro Espín Bedón [a,*], John R. Elliott [a], Tim J. Wright [a], Susanna Ebmeier [a], Patricia Mothes [b], Milan Lazecky [a], Yasser Maghsoudi [a], Jack McGrath [a], Daniel Andrade [b]

[a] COMET, School of Earth and Environment, University of Leeds, Leeds, UK

[b] Instituto Geofísico – Escuela Politécnica Nacional, Quito, Ecuador

ARTICLE INFO

Keywords:
Ecuador
Inter-Andean valley
Velocity field
InSAR
Volcanoes
Tectonic faults

ABSTRACT

We present a survey of deformation in the Ecuadorian Inter-Andean valley and surrounding regions from satellite radar and GNSS between 2017 and 2023, including anthropogenic, tectonic, landsliding and volcanic processes. Major anthropogenic signals include urban subsidence associated with water and resource extraction in Quito (−3.5 mm/yr), Cañar (+1.8 mm/yr) and Guayaquil (+~8 mm/yr). We also observe significant horizontal deformation caused by the interaction between the subduction zone and active tectonic faults. Four of Ecuador's 21 continental volcanoes are actively deforming and we also observed the continued subsidence of old volcano-sedimentary deposits in the northeast of the city of Cuenca. We examine the portion of the Chingual-Cosanga-Pallatanga-Puna right-lateral fault (CCPP) between the cities of Pallatanga and Riobamba and determine the geodetic slip rate and strain rate of this particular segment of the fault system and subsequently compare it with previously estimated geological slip rates. We estimated a slip rate of 3.1 ± 0.6 mm/yr, with shear strain ranging from 50 to 100 nst/yr, extending beyond the primary fault trace. Furthermore, shear strain extends southeastward (within a range of 16–30 km), where significant active branches of this complex fault system exist, with a slip rate of 2.7 ± 0.3 mm/yr. This study highlights specific areas for future monitoring of geohazards and infrastructure resilience in Ecuador, with particular relevance for similar Andean settings.

1. Introduction

Subduction zones, where tectonic plates converge, cause compression, uplift, and mountain-building (Stern, 2002). This process generates magma, fueling volcanic activity (Perfit et al., 2000; LaFemina, 2015), and leads to earthquakes and crustal changes due to stress release (Rikitake, 1976; Choy and Kirby, 2004; Ruff, 2013; Elliott et al., 2016). These dynamics link tectonics with mountain growth, volcanism, and landscape evolution (Kennan, 2000; Schellart, 2007; Huntington and Klepeis, 2017; Palin and Santosh, 2021).

Geodetic measurements, crucial for understanding Earth's current surface deformation and assessing natural hazards, utilize advanced technologies like Global Navigation Satellite Systems (GNSS) and Interferometric SyntheticAperture Radar (InSAR) (Krüger et al., 1994; Hofmann-Wellenhof et al., 2007; Herring et al., 2016). GNSS provides precise point measurements with high accuracy (Jarrin et al., 2022, 2023; Richter et al., 2016; Stamps and Kreemer, 2024), while InSAR offers broader coverage with lower precision (e.g. Weiss et al., (2019)). Integrating GNSS and InSAR data offers a comprehensive understanding of surface deformation, aiding in the estimation of strain rates and fault dynamics (Chlieh et al., 2004; Daout et al., 2016, 2019, 2023; Dodds et al., 2022; Grandin et al., 2012; Parizzi et al., 2021; Weiss et al., 2020).

Ecuador, located on the Pacific coast of northwestern South America (Fig. 1), is significantly influenced by the subduction of the Nazca plate beneath the South American continent, with a convergence rate of 55–58 mm/yr (Trenkamp et al., 2002; Nocquet et al., 2014; Alvarado et al., 2016). This tectonic activity leads to intense seismic events, such as the 2016 M_w 7.8 Pedernales earthquake that ruptured the subductive megathrust and the 1859 M_w 7.2 Quito thrust faulting earthquake considered a deep event within the subducting slab beneath the Andean Range (Beauval et al., 2010). The largest subduction event recorded was the 1906 Esmeraldas ~8.8 magnitude earthquake near the northern border with Colombia (Kanamori and McNally, 1982).

The interaction between the Nazca plate, the South American plate,

* Corresponding author.
E-mail address: eepabe@leeds.ac.uk (P.A. Espín Bedón).

https://doi.org/10.1016/j.jsames.2025.105588
Received 17 October 2024; Received in revised form 12 May 2025; Accepted 18 May 2025
Available online 27 May 2025

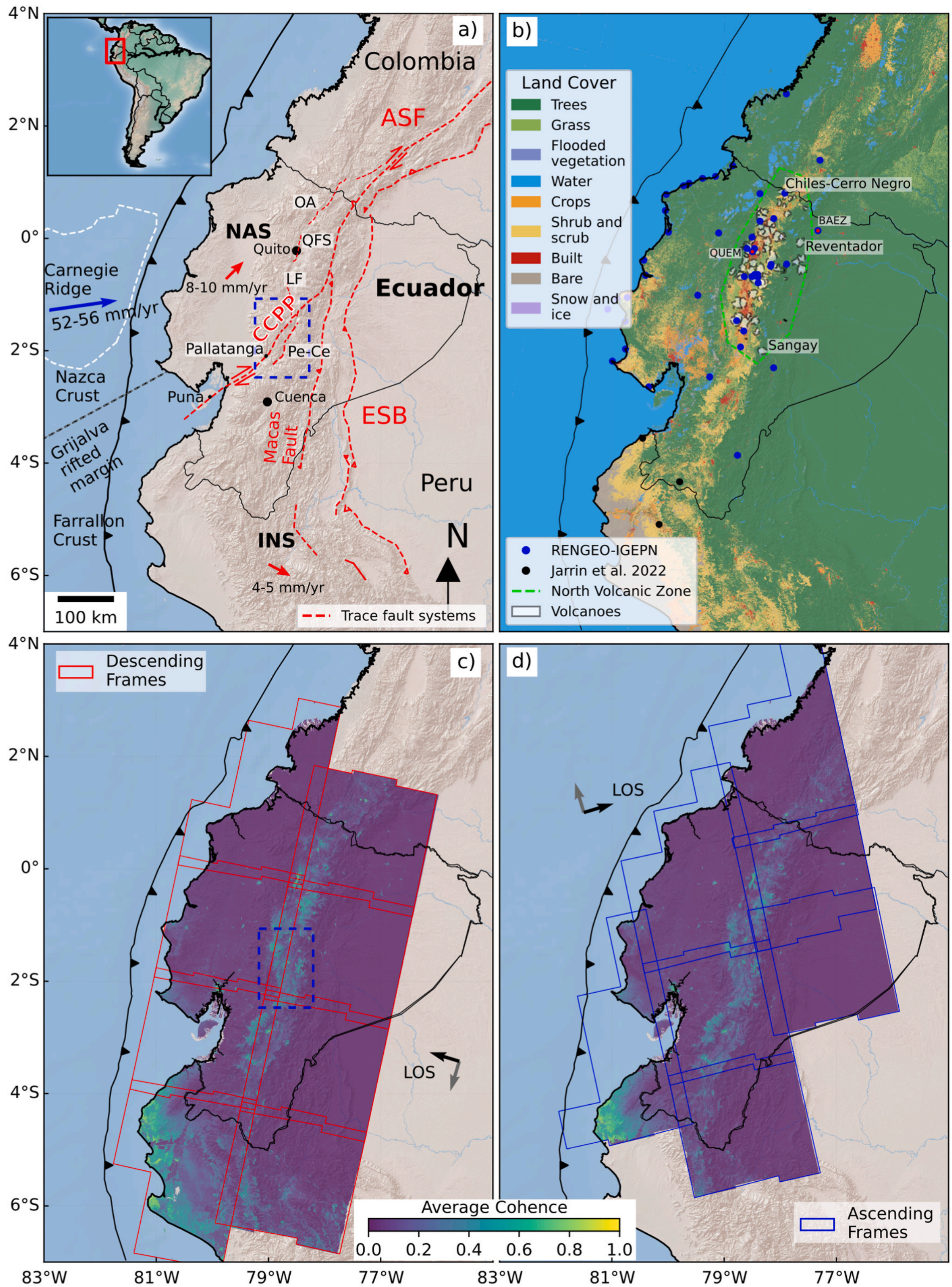

Fig. 1. a) Tectonic Setting of the Ecuadorian Subduction zone and the Andean Cordillera. The blue arrow indicates the direction of motion of the oceanic subducting Nazca towards South American plate (Nocquet et al., 2014; Yepes et al., 2016; Jarrin et al., 2022). Red arrows illustrate the motion of the North Andean Sliver (NAS) and Inca Sliver (INS) relative to South America (Nocquet et al., 2014; Villegas-Lanza et al., 2016; Jarrin et al., 2023). Abbreviations, CCPP: Chingual-Cosanga-Pallatanga-Puna Fault System, ASF: Afiladores-Sibundoy Fault, ESB: Eastern Sub-Andean Belt; QFS: Quito Faults System; LF: Latacunga Fault; OA: Otavalo-El Angel Fault system, Pe-Ce: Peltetec-Cebada dextral faults. The blue dashed square delineates the area between the cities of Pallatanga and Riobamba, where our focus lies and where we estimate the interseismic slip rate for short distances/wavelengths. b) Land cover map (based on Sentinel-2 data, from Brown et al. (2022)) with the GNSS network locations overlaid: blue dots represent the National network of GPS (RENGEO), while black dots denote GNSS from Jarrin et al. (2022), complementing the southern part of Ecuador. The green oval polygon delineates the North Volcanic Zone (NVZ) in Ecuador, and the white areas indicate the presence of some Holocene volcanoes. Average mean InSAR coherence from the c) Descending and d) Ascending Sentinel-1 interferograms. Blue and red outline boxes (c, d) delineate the extent of the Sentinel 1 LiCSAR frames. (For interpretation of the references to colour in this figure legend, the reader is referred to the Web version of this article.)

and the Carnegie Ridge (Fig. 1a) has created two tectonic blocks: the North Andean Sliver (NAS), moving at 8–10 mm/yr, and the Inca Sliver (INS) moving at 4–5 mm/yr (Nocquet et al., 2014; Alvarado et al., 2016; Villegas-Lanza et al., 2016; Jarrin, 2021). The NAS is bounded by the Chingual-Cosanga-Pallatanga-Puná fault system, extending from the Gulf of Guayaquil to Colombia (Baize et al., 2015; Alvarado et al., 2016). This fault system slips at rates of 2–7.6 mm/yr (Nocquet et al., 2014; Arias-Gallegos et al., 2023). Other significant faults include the Quito fault system (Alvarado, 2012; Alvarado et al., 2014; Mariniere et al., 2020; Reyes et al., 2020), the Latacunga fold-and-thrust belt system (Lavenu et al., 1995b), and the Otavalo-El Angel strike-slip fault system to the north (Yepes et al., 2016; Jarrin, 2021).

Ecuador's diverse land cover introduces unique challenges to geodetic studies, particularly those relying on InSAR data. Dense vegetation, prevalent in the Amazonian and Coastal regions, significantly reduces coherence at C-band due to radar wave scattering and absorption. This decorrelation is amplified by vegetation water content and soil moisture, which can bias deformation measurements in interferograms with short temporal baselines (Ansari et al., 2021; Maghsoudi et al., 2021; Purcell et al., 2022). These environmental factors interact with the tectonic processes to create a complex setting for precise deformation monitoring, requiring advanced processing techniques (Westerhoff and Steyn-Ross, 2020; Cao et al., 2022).

Volcanism in continental Ecuador exemplifies the interplay between tectonics and geological processes, driven by the subduction of the Nazca plate beneath the South American plate. This process forms the Ecuadorian segment of the Northern Andean Volcanic Zone (NVZ), a 350 km arc comprising 84 Plio-Quaternary volcanoes (Ramon et al., 2021; Bablon et al., 2019). The volcanoes, varying in petrographic, geochemical, and eruptive characteristics, are classified by activity into 1) extinct, 2) potentially active, 3) active, and 4) in eruption (Santamaria 2017; Ramon et al., 2021; Instituto Geofísico, 2024). These volcanic systems, influenced by the tectonic framework, further underscore the intricate relationship between Ecuador's geodynamics and its landforms (Hall et al., 2008).

Surface deformation maps are essential for providing crucial information by detecting subtle changes in ground elevation or horizontal displacements and identifying potential hazards associated with tectonic activity (Elliott et al., 2016; Elliott, 2020), volcanic processes (Biggs et al. 2017; Poland and Zebker, 2022; Lundgren and Bato, 2021), and anthropogenic effects such as groundwater extraction (e.g. Hussain et al. (2022) and Babaee et al. (2024)) or mining (e.g. Chen et al. (2021) and Declercq et al. (2023)). The value of InSAR extends across various global regions, where it has been employed to monitor volcanic systems, providing crucial data on magma chamber inflation and deflation. For example, significant findings have been reported in Iceland (Pedersen and Sigmundsson, 2006; Ofeigsson et al., 2011), Hawaii (Kundu et al., 2020; Bemelmans et al., 2021), and in detecting pre-eruptive signals at Agung volcano (Bemelmans et al., 2023). InSAR-based deformation maps also have significantly enhanced our understanding of fault dynamics and the associated seismic hazards. For instance, studies of the San Andreas Fault in California (Fialko, 2006; Scott et al., 2020), the creeping behaviour along the Haiyuan Fault in China (Jolivet et al., 2013), and interseismic coupling in subduction zones in Mexico (Maubant et al., 2022) illustrate the critical role of these maps in advancing our knowledge of seismic activity.

In Ecuador, the Instituto Geofísico has strengthened these efforts through the National Geodesy Network (RENGEO), comprising 85 permanent GNSS stations (Alvarado et al., 2018; Mothes et al., 2018). This network supplies crucial data on phenomena such as the NAS velocity (Nocquet et al., 2014; Alvarado et al., 2016; Jarrin, 2021; Jarrin et al. 2022, 2023; Arias-Gallegos et al., 2023), interseismic coupling (Chlieh et al., 2014), postseismic deformation (Nocquet et al., 2017; Twardzik et al., 2019), and slow slip events in the Ecuadorian subduction zone (Rolandone et al., 2018; Vaca et al., 2019). Complementing these efforts, InSAR data have advanced the understanding of tectonic deformation in the central-northern region of Ecuador and southern Colombia between 2017 and 2023 (Marconato et al., 2024a). However, unlike this investigation, our study emphasizes the integration of diverse datasets to capture both short-and long-wavelength deformation phenomena, thus contributing novel insights into volcanic, tectonic, and anthropogenic processes across Ecuador. We stress that INSAR studied in the Ecuadorian territory contribute to studies of tectonic faults (e.g., Pisayambo (Champenois et al., 2017), Pallatanga (Baize et al., 2015; Marconato et al., 2024b), Quito Fault system (Espín et al., 2018; Mariniere et al., 2020), subduction earthquakes (e.g., Pedernales earthquake (Béjar-Pizarro et al., 2018; Chalumeau et al., 2021)), volcanic deformation (Ebmeier et al., 2016; Mirzaee and Amelung, 2017; Espín Bedón et al., 2022; Espín Bedón et al., 2024), and mining subsidence (e.g., Zaruma City, Cando Jácome et al., 2020).

A comprehensive large-scale deformation map is crucial for overcoming the limitations of localized studies and providing a broader perspective for monitoring tectonic and volcanic activity. For example, strain rate maps across the entire Alpine-Himalayan Belt enhance the understanding of seismic hazards (Hooper et al., 2020), contribute to the analysis of slow slip events on a regional scale in Mexico (Maubant et al., 2020), and improve insights into magmatic processes, as demonstrated by extensive surveys in the East African Rift System (Albino and Biggs, 2021) or Turkish volcanoes (Biggs et al., 2021). In Ecuador, the creation of a nationwide deformation map is crucial for filling the gaps left by localized analyses and for offering a thorough understanding of the region's geodynamic activity. Such a map would not only enhance our comprehension of the tectonic and volcanic processes at play but also improve hazard assessment and disaster preparedness on a national scale. By systematically mapping deformation throughout Ecuador, it will be possible to identify previously unknown areas of concern, better assess risks in populated regions, and inform infrastructure development and land use planning with real-time data.

Here, we use radar (SAR) data from the European Space Agency's (ESA) Sentinel-1 C-band satellite to generate a line-of-sight time series and measure displacements across Ecuador in both ascending and descending tracks. Additionally, we use the GNSS time series recorded by RENGEO stations to estimate the velocity components. By integrating the InSAR time series spanning 6 years with the GNSS data between December 2017 and August 2023, we produce high-resolution surface east-west and vertical velocity data for Ecuador at a general scale of 250 m. This approach demonstrates the potential of comprehensive frame coverage to capture tectonic, volcanic, and anthropogenic deformation phenomena. Specifically, we use vertical component data from both ascending and descending tracks to identify deforming areas related to volcanic activity, subsidence from mining or groundwater extraction, and, additionally, to estimate the interseismic slip rate and strain rate in the Pallatanga area (blue dashed square in Fig. 1a) capturing short-wavelength deformation in the shallow crust, while long-wavelength signals in the deeper crust and lithosphere reflect the interseismic period with traces of postseismic deformation.

2. Ecuador country-scale velocity field and components of motion: data and methodology

2.1. Identification of the interseismic period following the Pedernales earthquake

We determined the interseismic period following the postseismic phase caused by the Pedernales earthquake manually/empirically by identifying the boundary where one ends and the other begins in the GPS station data (e.g., QUEM and ESMR stations, Supplementary Figs. S1 and S2). This was achieved by seeking a constant velocity in the East component. To accomplish this, we began our linear trend analysis on the time series, varying the start date for the linear regression from June 2017 onwards, and estimating the RMS for each month's start. The lowest RMS was found for the start of December. This approach provides the interseismic period for the shallow crust, as reflected in the short-wavelength deformation. In contrast, the deeper crust and lithospheric deformation, which is associated with long wavelengths, continues to show the interseismic period but contains a remnant of postseismic deformation that persists to the present day.

2.2. Sentinel-1 data and InSAR processing

We measure 6.1 years of ground displacement across Ecuador using InSAR time series from ~2470 Sentinel-1 SAR acquisitions. We create ~19,147 unwrapped geocoded interferograms and coherence data at 56 m resolution using the Looking Into Continents from Space with Synthetic Aperture Radar (LiCSAR) system (Lazecký et al., 2020). We create short and longer interferograms with time spans of 6, 12, 24 days and 1, 2, 3, 6, 9 months, and 1 year in between each epoch (Supplementary Fig. S3) using the GAMMA software (Werner et al., 2000) (Note that, since December 2021, due to the failure of Sentinel-1B, it has not been possible to form 6-day interferograms).Subsequently, we analyse the most effective strategy for combining these interferograms to construct our final time series, following the approach outlined by Espín Bedón et al., (2024), in the relevant area (Section 3.1), and finally we use only interferograms with a time span of 12 days or more. We used the Copernicus DEM data set to remove topographic phase contributions (European Space AgencySinergise, 2021). The interferograms are multilooked by a factor of 20 in range and 4 in azimuth during the processing. For our analysis, we use fifteen LiCSAR frames of approximately 250 km by 250 km extent (7 ascending (Supplementary Table S1) and 8 descending (Supplementary Table S2), as shown in Fig. 1c and d) that cover the entire country using data acquired between November 2017 and August 2023. We focus on this period because we have complete data coverage for both tracks during that time.

We estimate the line-of-sight (LOS) velocities and time series for each frame (Fig. 2) using the LiCSBAS approach (Morishita et al., 2020; Lazecký et al., 2024) that estimates ground displacements at acquisition epochs on a pixel-by-pixel basis from the network of interferograms. Subsequently, we downsample our interferometric data from ~56 m to ~250 m resolution to decrease processing demands while preserving adequate resolution for detect ing tectonic deformation signals (e.g. Watson et al., (2022)). Secondly, we mask out and remove pixels with an average coherence of less than 0.05. This threshold primarily excludes vegetated areas, such as the Amazonian region. We test an atmospheric correction approach using the Generic Atmospheric Correction Online Service (GACOS) correction (Yu et al., 2018).

GACOS uses numerical weather models (European Centre for Medium-Range Weather Forecasts (ECMWF) data) to predict atmospheric phase delays. We observed that the quality of the interferograms, as evaluated by phase standard deviation, deteriorated following the correction (e.g. Supplementary Fig. S4), this decline may be attributed to the influence of steep topography on local water vapour distribution and hydrostatic pressure, as well as the limited availability of ECMWF input data in the region (e.g. Dogru et al., 2023. and Espín Bedón et al., (2024)). We have decided not to proceed due to the degradation of correction in over 50 % of our interferograms.

In the next step, we identified and removed bad interferograms from

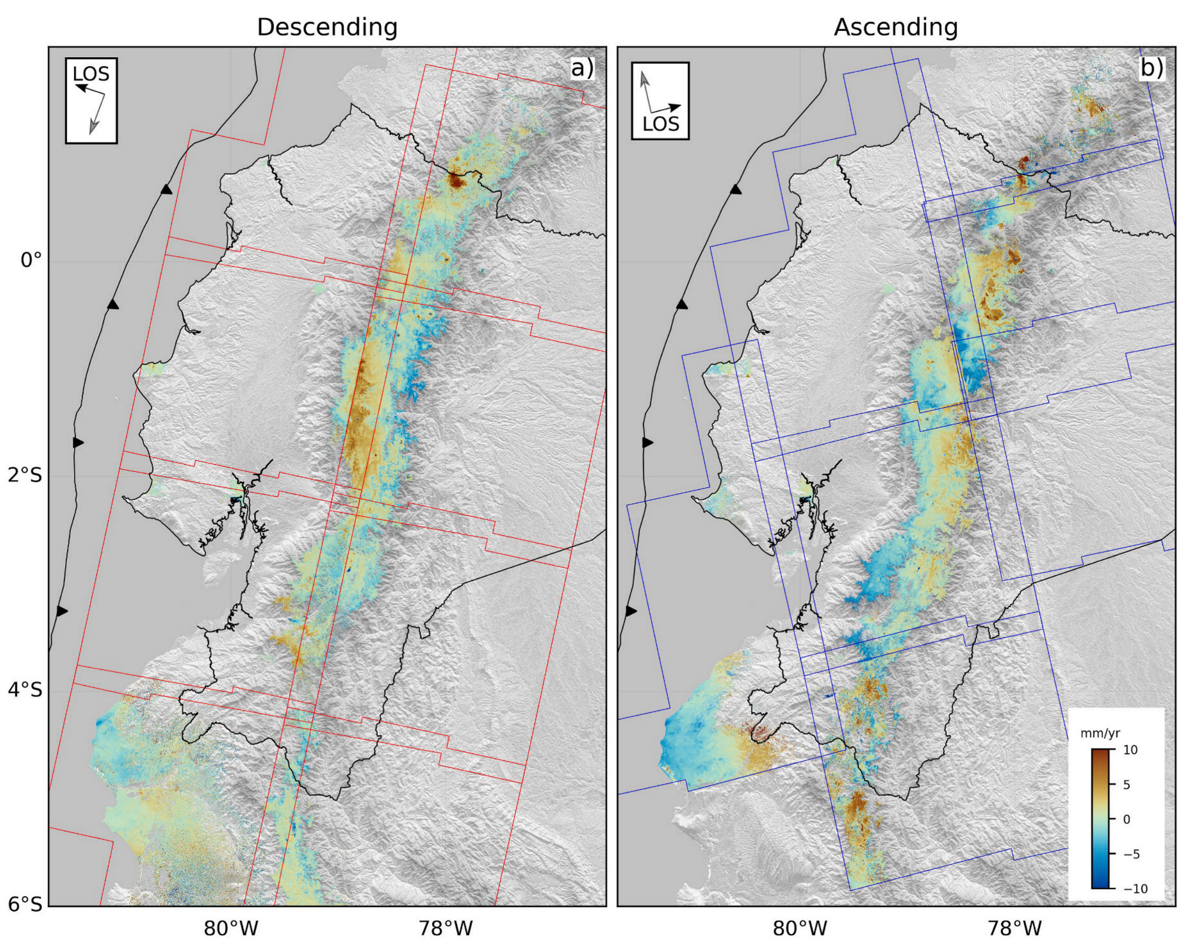

Fig. 2. Average line-of-sight velocities depicted for (a) descending and (b) ascending frames at a resolution of 260 m. Motion towards the satellite in the line-of-sight (LOS) is indicated in red, while motion away from it is denoted in blue. In this figure, each frame has its own distinct local zero velocity reference. Blue and red dashed outline boxes delineate the extents of the Sentinel 1 LiCSAR frames. (For interpretation of the references to colour in this figure legend, the reader is referred to the Web version of this article.)

the network based on quality statistics thresholds. We set a threshold of 0.3 (30 % coverage threshold) for unwrapping data to determine the minimum acceptable coverage of valid unwrapped pixels of interferograms and 0.05 for the average coherence. Furthermore, we identify errors in the unwrapping process by applying a phase closure technique (Biggs et al., 2007) pixel by pixel and drop unwrapped pixels with at least one erroneous loop closure (Lazecký et al., 2024) (e.g. Wang et al. (2024)). We ingest the improved and masked interferograms in the small baseline inversion approach (Morishita et al., 2020) to construct the time series. We use the bootstrapping method (Efron et al. 1986) to estimate the uncertainties associated with each LOS velocity (Supplementary Figs. S5 a,b).

We mask the remaining noisy pixels using a threshold derived from a statistical quality check (e.g. RMS of the residuals in the inversion, Morishita et al., 2020). We improve the signal-noise ratio of the data by employ ing spatio-temporal-filtering (Hooper et al., 2012), with a temporal window width of 18 days and a spatial width of 5 km (testing of filtering approaches shown in Supplementary Figs. S6 and S7). Finally, we apply a linear elevation-phase correction to subtract the topography-correlated component of the atmospheric signal, accounting for the lowest and highest elevation of each frame. The LiCSBAS input parameter settings used in this study are presented in Supplementary Table S3.

2.3. Fitting velocities for GNSS

We employ 48 sets of GNSS processing time series data sourced from RENGEO-IGEPN originally in the Nazca (NAS) reference frame (Mothes et al., 2013; Alvarado et al., 2018) and converted to the South American plate (SOAM) reference frame, covering the identical timeframe as our InSAR data (December 2017–August 2023). Furthermore, we integrate 6 GNSS velocities located in the southern region of Ecuador, referenced to the SOAM, as obtained from Jarrin et al., (2022). This facilitated coverage of the southern region of Ecuador during the GNSS time series period from 2008 to 2020 (Fig. 1b), where the effect of the Pedernales earthquake has been corrected (Jarrin et al., 2022). We adopt a least-squares approach to derive a model that accurately fits the East (E) and North (N) component of GNSS data (e.g. Arias-Gallegos et al., (2023); Blewitt et al., (2016); Jarrin, (2021); Jarrin et al., (2022); Liu et al., (2021)).

Our model incorporates a linear regression representing the overall trend, an annual oscillation, and offsets associated with earthquakes, as described by the following equation:

$$Y(t) = Vt + b + \sum_{i=2}^{n} H(t - t_i)C_i + [A\, sin(2\pi t) + B\, cos(2\pi t)] \quad (1)$$

where Y (t) represents the displacement as a function on time of the north and east components; V is the long-term linear deformation rate, t represents time, b is the reference position, H(*) is a Heaviside step function, C_i represents the coseismic deformation of each earthquake (n = 2 in this study, t_i is the event time), and A and B are the magnitudes of the seasonal signal.

Two major earthquakes were identified as events impacting all stations and time series for the period under study: 1) the earthquake that occurred on February 22, 2019 (magnitude M_w 7.5) in Palora-Ecuador, and 2) the earthquake on May 26, 2019 (magnitude M_w 8) in Peru (U.S. Geological Survey, 2023). Furthermore, a third event has been incorporated for June 6, 2021 in Manta (magnitude Mw 4.6). This earthquake was recorded and exclusively affected nearby stations, specifically SLGO, MHLA, MLEC, ISPT, SALN, AYAN, and CABP, particularly in the eastern component (refer to Supplementary Methods 9.1.1 and Figure Supplementary S8).

As well as estimating the velocities for the East and North components at each GNSS station (see Supplementary Table S4), we evaluate the quality of our data fit by estimating the root-mean-square (RMS) error between the observed data and the fitted model, as well as evaluating the differences between them (e.g. QUEM and BAEZ stations in Fig. 3 and Supplementary Fig. S8). We convert the velocities of the GNSS stations from within the NAS reference frame to that of SOAM (as presented in Table Supplementary S5) removing the trend predicted by the Euler pole defined by Jarrin (2021) to eliminate the plate movement and determine the surface displacements. Additionally, to constrain the edge for data interpolation at the eastern border of our GNSS network, we include 32 artificial boundary stations with zero velocity beyond 78°W, following the methodology proposed by Watson et al. (2022) (Supplementary Table S6). This assumption is based on the crustal stability and lack of movement of this area within the South American reference frame. Then, we interpolate the North and East GNSS velocities and artificial zero velocities (shown in Fig. 4c and d) using a universal kriging algorithm implemented with the PyKrige Python Package (Murphy et al., 2021). This generates a continuous velocity field that captures both local variations and broader spatial trends. We employed a Gaussian variogram model to achieve a continuous and smooth spatial pattern in our interpolation, in comparison to the spherical or exponential models (e.g. Ou et al. (2022) and Fang et al. (2022)).

2.4. Decomposed velocity fields

We employ the approach defined by Watson et al. (2022) for combining and decomposing our InSAR velocities and interpolated GNSS velocities into east (V_E) and vertical (V_U) velocity components (e.g. Hussain et al. (2016), Ou et al. (2022), and Wright et al. (2023)). Initially, the line-of-sight velocities obtained from each InSAR frame have their own independent references (Fig. 2). Therefore, we adjust the LOS velocities to the SOAM reference frame using the interpolated GNSS velocities (Fig. S21). To achieve this, we project the East and North GNSS velocities onto the satellite LOS direction. We subtract and determine the residual between our LOS GNSS and LOS InSAR velocities (e.g. Watson et al. (2022), Wright et al. (2023), Watson et al. (2024), and Wang et al. (2024)). We use a median filter for each InSAR frame (e.g. Xu et al. (2021) and Watson et al. (2022)) to smooth the residual and subtract it from the InSAR velocities to align them with the reference frame of the GNSS velocities (SOAM). We also refine the LOS uncertainties for each frame using a distance-dependent scaling factor based on a spherical model fit to correct the frame reference effect follow the method defined by Ou et al., (2022) (e.g. Fang et al., (2022); Watson et al., (2022)) (Suplementary Figure S5 c,d and S9). We merge along-track using the median function in the overlapping LOS velocities by subtracting the difference of the median values between tracks.

We estimate vertical (V_U) and east-west velocities (V_E) at a pixel scale of approximately 250 m, incorporating the interpolated North GNSS velocities and their associated uncertainties into our decomposition. We solve for V_E and V_U using weighted least squares and the data variance-covariance matrix (VCM) (Watson et al., 2022). The correlation between InSAR and GNSS V_E exhibits an R^2 value of 0.5 and a root mean square (RMS) of 1.9 mm (Figure Supplementary S10). The uncertainties associated with the decomposed velocities (Supplementary Fig. S12 and Supplementary information 9.2) typically range from 0.1 to 1.7 mm/yr in the east component and from 0.3 to 1.4 mm/yr in the vertical component. Lowest uncertainties are found in the regions where tracks overlap. We have grouped and estimated the standard deviation in the overlap areas (e.g. Watson et al. (2022)), with values ranging from 1.3 to 1.9 mm/yr for the descending track and from 1.4 to 2.2 mm/yr for the ascending track. However, significantly higher values are observed near the Chiles volcano, where the standard deviation reaches 5.60 mm/yr, due to volcanic activity and the earthquake that occurred on 25 July 2022. Regarding the across-tracks overlap (between frames on different tracks), the standard deviation is observed to be 2.4 mm/yr for the descending track and 1.7 mm/yr for the ascending track (Supplementary Fig. S11). Next, we decompose to the vertical and horizontal components of the uncertainties in the along-track zones

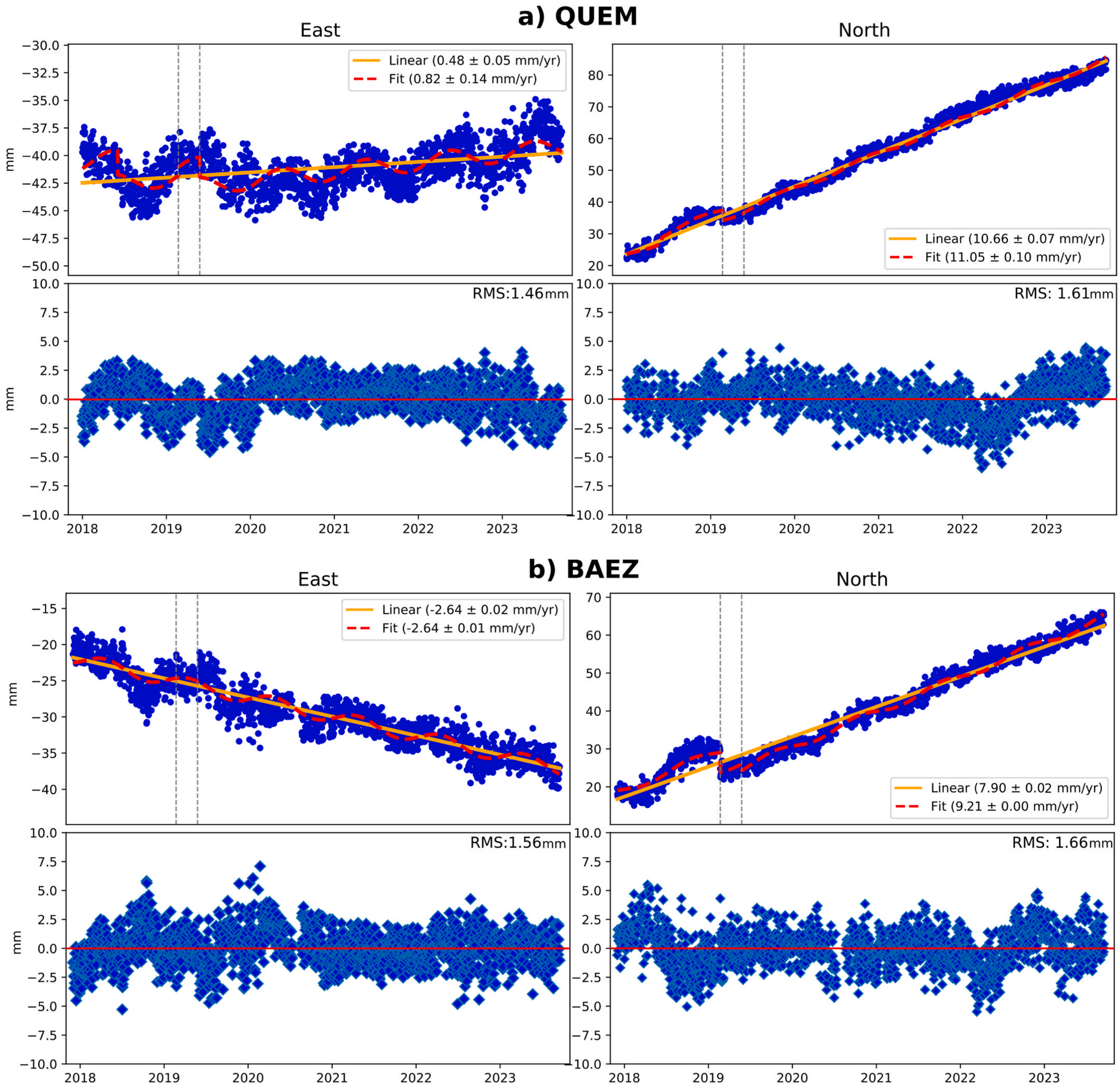

Fig. 3. Examples of the fitted time series and root mean square (RMS) values for the east and north components at two stations using equation (1): a) QUEM and b) BAEZ (see location in Fig. 1b). The dotted red line represents the data fit, the orange line represents the linear term rate, and the dotted grey vertical lines indicate fixed offsets for the two earthquakes: February 22, 2019 (M_w 7.5) in Palora-Ecaudor and May 26, 2019 (M_w 8) in Peru (U.S. Geological Survey, 2023). Note that the plotted uncertainties are formal uncertainties derived from the linear fit to many points. (For interpretation of the references to colour in this figure legend, the reader is referred to the Web version of this article.)

using the incidence angle and the heading of each track, respectively (Supplementary Fig. S13).

3. Ecuador country-wide surface velocity: results

The overall measured vertical velocities of the country (Fig. 5) are primarily influenced by volcanic deformation, such as Cayambe (Butcher et al., 2021; Espín Bedón et al., 2022) (Fig. 5b), Sangay (Hidalgo et al., 2022; Espín Bedón et al., 2024) (Fig. 5e), and Guagua Pichincha (Yepez et al., 2020; Mirzaee et al., 2023) (Fig. 5j), as well as tectonic-volcanic deformation, like Chiles-Cerro Negro (Gómez Cruz, 2020; Mirzaee et al. 2021) (Fig. 5a). Subsidence or contraction in volcano deposits is observed in the northeastern ravine of the Tungurahua Volcano (Fig. 5d) and Reventador volcano (Fig. 5m). In addition, subsidence can be observed in cities such as Guayaquil (Fig. 5h), southern Quito (Fig. 5i), and Cañar (Fig. 5g). There are also effects of mining to the north of Quito (Fig. 5k). In the coastal region where coherence and deformation data are very limited, only a small area and amount of uplift is observed in the city of Manta (5q). Furthermore, subsidence occurs in volcanic sediments deposits between Cuenca and Azoguez in the south (Fig. 5f). The CCPP fault system (Fig. 5l) does not exhibit significant vertical deformation.

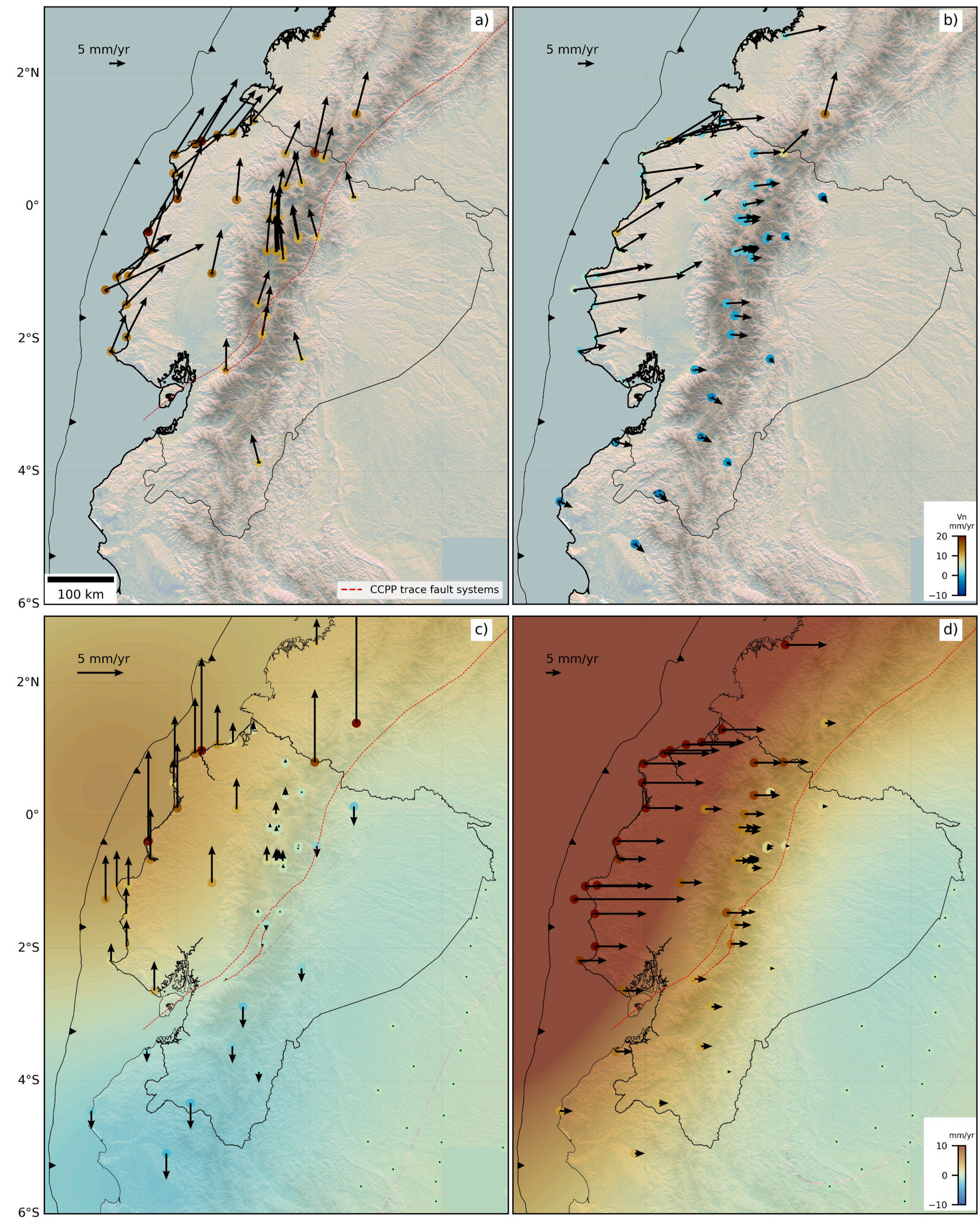

Fig. 4. GNSS horizontal velocities depicted as arrows. a) with respect to NAS; b) with respect to stable South America plate (SOAM). Spatially interpolated GNSS velocities were generated by using a universal kriging algorithm for c) North (V_N) and d) East (V_E) components with respect to SOAM. GNSS components are shown in coloured dots respectively. Red dashed line shows the trace of the CCPP: Chingual-Cosanga-Pallatanga-Puna Fault System. (For interpretation of the references to colour in this figure legend, the reader is referred to the Web version of this article.)

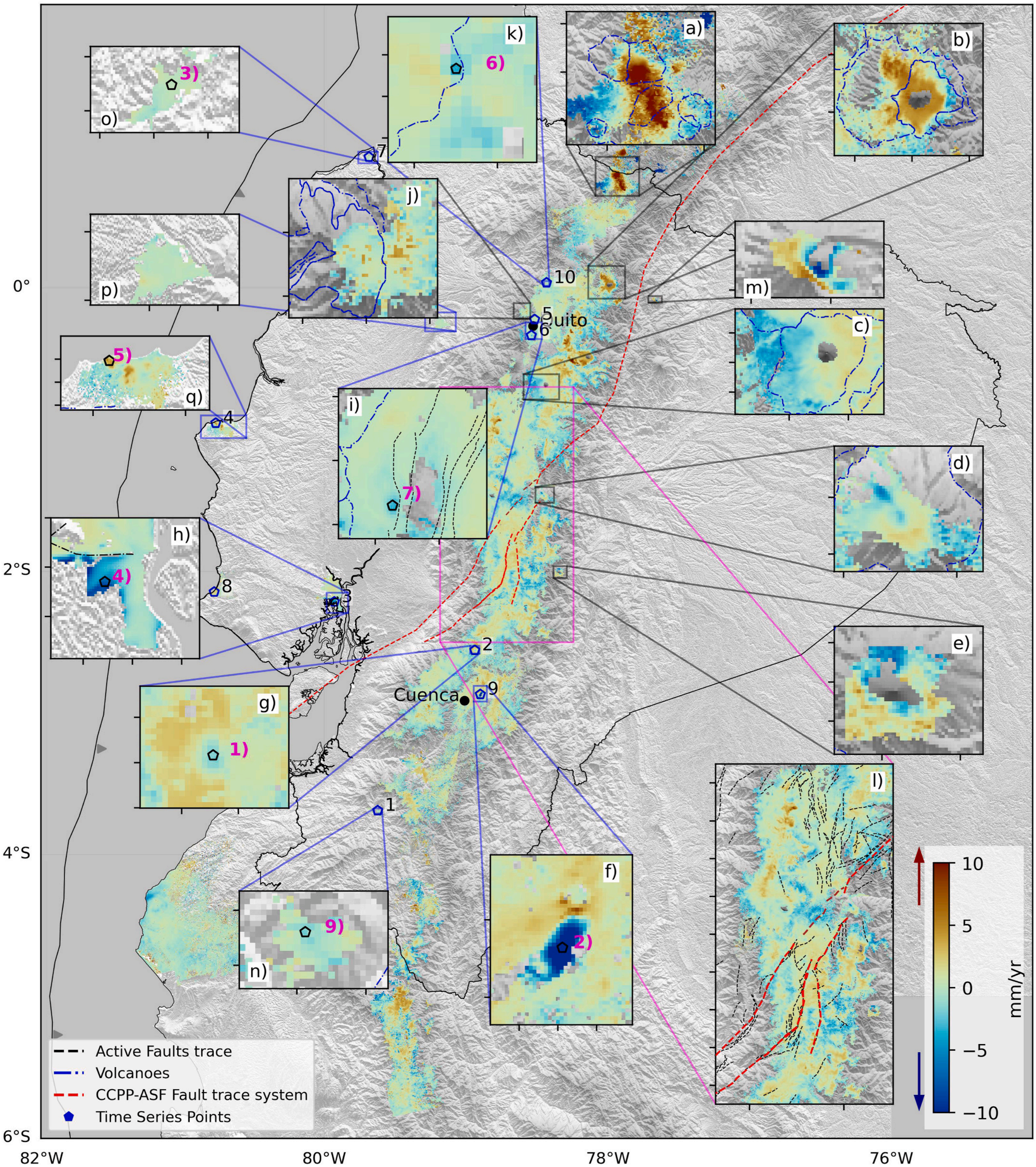

Fig. 5. Vertical velocity from the velocity field decomposition shows the deformation related to tectonic-volcanic activity: a) Chiles-Cerro Negro; Volcanoes: b) Cayambe; c) Cotopaxi; e) Sangay; j) Guagua Pichincha, m) Reventador; as well as anthropogenic processes such as subsidence in: d) Tungurahua ravine; f) Tarqui volcanic deposits; g) Cañar city; h) Guayaquil city; i) Southern Quito city; k) North Quito sand mining; n) Zaruma city and l) represents the area of CCPP that is the eastern boundary and is associated with the relative movement of the NAS. In the coastal area we have deformation zones identified only in the cities where coherence is maintained: o) Esmeraldas, p) Santo Domingo and q) Manta. The dashed red line is a simplified representation of major fault CCPP. The color palette in the middle left corresponds to the scale of the zoomed-in subplots, while the one in the lower left corresponds to the entire map of the country. The magenta numbers and blue markers indicate the cumulative time series points for the anthropogenic deformation signals. Active fault trace from Alvarado et al. (2014). (For interpretation of the references to colour in this figure legend, the reader is referred to the Web version of this article.)

The horizontal velocity (Fig. 6) demonstrates a general east-west gradient, illustrating how ongoing convergence and the locked behaviour of the subduction interface deforms the entire country. Higher velocities are observed in coastal cities and in the northern region of the CCPP, as opposed to the southern region (Fig. 6i), as indicated by GNSS studies (e.g. Nocquet et al. (2014), Jarrin (2021), Jarrin et al. (2022), and Arias-Gallegos et al. (2023)). However, a noticeable deformation associated with the fault system further south, including the Guamote, Cebada, and Peltetec faults, is also observable (Fig. 6l). This deformation likely represents the effects of interseismic slip, which may not have been captured in GPS studies due to limitations in coverage compared to that of the InSAR methodology and also the lack of stations installed in this sector. Additionally, clear deformation is observed in volcanic regions such as Sangay (Fig. 6e), Chiles-Cerro Negro (Fig. 6a), and Cotopaxi (Fig. 6c). Notably, only the Holocene volcanic areas exhibit clear horizontal deformation (Fig. 6f). In the following sections we discuss the deformation sources in more detail.

3.1. Volcanic activity (December 2017–August 2023)

Volcanic activity during this period in Ecuador has been characterized by three erupting volcanoes: Reventador, Sangay and Cotopaxi. In the same time period, the Chiles-Cerro Negro volcanic complex exhibited seismic activity that exceeded the typical thresholds associated with normal volcanic behavior, indicating a possible state of unrest. The specific references for each volcano's activity are summarized in Supplementary Table S7. The identification of deformation in line-of-sight (LOS) measurements for both tracks reveal uplift associated with Sangay Figs. 5 and 6 e) (e.g. Espín Bedón et al., (2024)) and Chiles-Cerro Negro volcanic centers (Fig. 5 a), and subsidence in Reventador (Fig. 5 m).

In the Chiles-Cerro Negro area (Figs. 5 and 6 a), which encompasses the Potrerillos region to the southwest, we observe maximum uplift rates of approximately ~15 mm/yr. Yepez et al. (2021) reported a maximum line-of-sight (LOS) deformation of 2.5–3 cm/yr in the area between 2014 and 2019, which they interpreted as uplift. However, in our analysis of the east-west component, we identify a significant deformation of ~6 mm/yr towards the east in the area between the Chiles-Cerro Negro volcano and Potrerillos. This deformation is probably associated with the hydrothermal system in the region (Sierra, 2015; Ebmeier et al., 2016; Gómez Cruz, 2020; Yepez et al., 2021; Mirzaee et al. 2021). This area is also affected by seismic activity, including a Mw 5.6 earthquake on 25 July 2022 with depth 2 km (Instituto Geofísico IG-EPN, 2022) (Supplementary Fig. S14a).

Sangay exhibits a maximum uplift rate of approximately 9 mm/yr, accompanied by horizontal movement (Figs. 5 and 6e), with the western flank shifting westward at a rate of 10 mm/yr, and the eastern flank moving east-ward at approximately 12 mm/yr, predominantly associated with the new activity initiated in 2019 and persisting until 2023 (Vasconez et al., 2022; Hidalgo et al., 2022; Espín Bedón et al., 2024). Furthermore, the horizontal component indicates that the deformation on the southeast flank would be related to the new deposits and the movement of the older deposits on this flank (Espín Bedón et al., 2024). Reventador exhibits subsidence (Fig. 5m and Supplementary Fig. S14b), potentially linked to the compaction of volcanic deposits (Arnold et al., 2017; Instituto Geofisico, 2020). Tungurahua is subsiding in the area of the pyroclastic deposits from 2013 to 2016 (Fig. 5d and Supplementary Fig. S14d) (Hall et al., 2015), which can be attributed to the contraction/compaction of these deposits (e.g Naranjo et al. (2016) and McAlpin et al. (2017)). Cotopaxi displays a minor westward movement pattern, consistent with observations made by Morales et al. (2017).

Regions of vertical deformation were also observed in volcanic centers that did not culminate in eruptions, as exemplified by Guagua Pichincha, which displayed inflation (as also reported by Yepez et al. (2020) and Mirzaee et al. (2023)). Cayambe volcano exhibits inflation around its edifice at a rate of approximately 4 mm/yr in the southeast direction (as reported by Espín Bedón et al. (2022)) between 2015 and 2019 (Fig. 5 b). There have been no reports of heightened gas emissions or seismic activity during the study period for either volcano, and no distinct deformation in the east-west direction was observed throughout the study period.

3.2. Anthropogenic-related deformation

We have identified seven distinct locations that exhibit significant vertical velocities associated with non-tectonic processes. Three of these are related to cities experiencing subsidence: Guayaquil (Fig. 5h), Cañar (Fig. 5g), and Zaruma (Fig. 5n), as well as the southern portion of Quito (Fig. 5i). Subsidence signals occurred in zones composed by volcano-sedimentary substratum to the east of Cuenca (Fig. 5g), and to the north of Quito in the San Antonio de Pichincha sector (Fig. 5k).

We have extracted time series at each location for both ascending and descending tracks, using a local reference pixel within the area of the anthropogenic signals (Supplementary Fig. S15). Each ascending and descending LOS series was first compared by aligning the dates, followed by interpolation using a weekly interval (7 days) for the common dates. Additionally, a linear trend was estimated to closely match the initial un-interpolated LOS data (e.g. Supplementary Fig. S16). Finally, the combination was performed using the same method described by Wright et al. (2004), resulting in the time series for both the vertical and horizontal (east-west) components for each area (Fig. 7).

The Zaruma time series illustrates a vertical velocity of −3.3 mm/yr (−2.6 and −1.3 mm/yr LOS rates for the descending and descending trajectories, respectively, Supplementary Fig. S15i). The most significant deformation is observed between 2018 and mid-2021. Cando Jácome et al. (2020) correlate this subsidence, occurring from 2016 to 2019, with mining activity in the region.

In the case of Guayaquil, the area of most pronounced deformation is situated in the southwest (Fig. 5h), exhibiting a significant vertical displacement of −7 to −8.8 mm/yr. This trend persists steadily from 2018 to 2023 (Fig. 7d), characterized by a linear velocity in Line-of-Sight (LOS) measurements of −6.2 (descending) and −3.6 mm/yr (ascending) (Supplementary Fig. S15d). This deformation is likely attributable to the compression of clay deposits (Cuervas-Mons et al., 2021; Carrillo Bravo et al., 2021).

In the city of Cañar, a subsidence rate of −1.8 mm/yr is observed in the decomposed vertical velocity (Fig. 5g), with a consistent trend of −3.6 mm/yr in the ascending track and - 1.8 mm/yr in the descending track (Supplementary Fig. S16a). Our interpolated vertical series shows a subsidence rate of −3.8 mm/year (Fig. 7a). Despite the absence of reports or studies addressing the causes of this deformation, geological maps suggest a potential correlation with with the city's infrastructure and the terrain type, specifically lake and river terraces (Bourgois et al. 2006).

The city of Manta experiences uplift ranging between 1 and 5 mm/yr in the decomposed vertical velocity (Fig. 5q). The interpolated series of components shows a subsidence of 3.5 mm/yr (Fig. 7e). The time series reveal a linear LOS velocity of 3.3 mm/yr in the descending track and 1.7 mm/yr in the ascending track (Supplementary Fig. S15e). This uplift may be linked to the marine formation, estimated by Pedoja et al. (2006, 2009) and Cisneros Medina (2017) due to active tectonic activity in the northern region and erosion on the Manta peninsula.

In the Quito area, we have extracted a time series in the southern Santo Tomas sector (Fig. 5i), where the area exhibits subsidence, with a maximum rate of −3.5 mm/yr (Fig. 7g). The time series in LOS indicates a constant linear velocity of −1.9 mm/yr in the descending track and −3.4 mm/yr in the ascending track (Supplementary Fig. S16g). The signal found along the reverse fault boundary at the edge is sharp, becoming smoother to the north, which may indicate a fault-controlled water aquifer. The hydrological model of the city of Quito in the south shows that this zone is affected by the reverse faulting and may be the

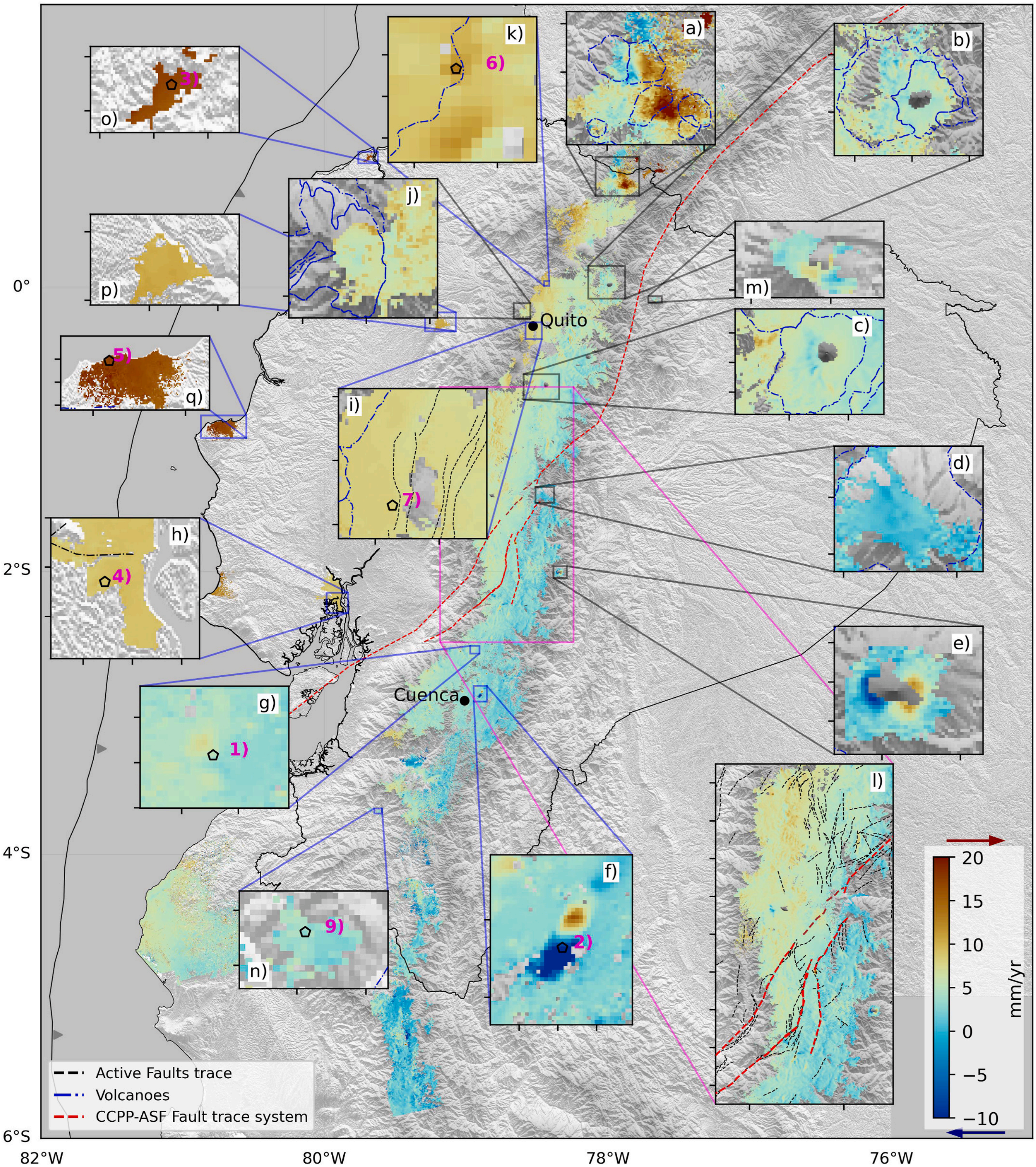

Fig. 6. Decomposed East-West velocity shows the deformation related to tectonic-volcanic activity: a) Chiles-Cerro Negro; Volcanoes: b) Cayambe; c) Cotopaxi; e) Sangay; j) Guagua Pichincha, m) Reventador; subsidence in volcano deposits: d) Tungurahua ravines; as well as anthropogenic processes such as subsidence in: f) Tarqui volcanic deposits; g) Cañar city; h) Guayaquil city; i) Southern Quito city; k) North Quito sand mining; n) Zaruma city; and l) represents the area of CCPP that is the eastern boundary and is associated with the movement of the NAS. In the coastal area we have deformation zones only in the cities: o) Esmeraldas, p) Santo Domingo and q) Manta. The dashed red line is a simplified representation of major fault CCPP. The color palette in the middle left corresponds to the scale of the zoomed-in subplots, while the one in the lower left corresponds to the entire map of the country. Active fault trace from Alvarado et al.(2014). (For interpretation of the references to colour in this figure legend, the reader is referred to the Web version of this article.)

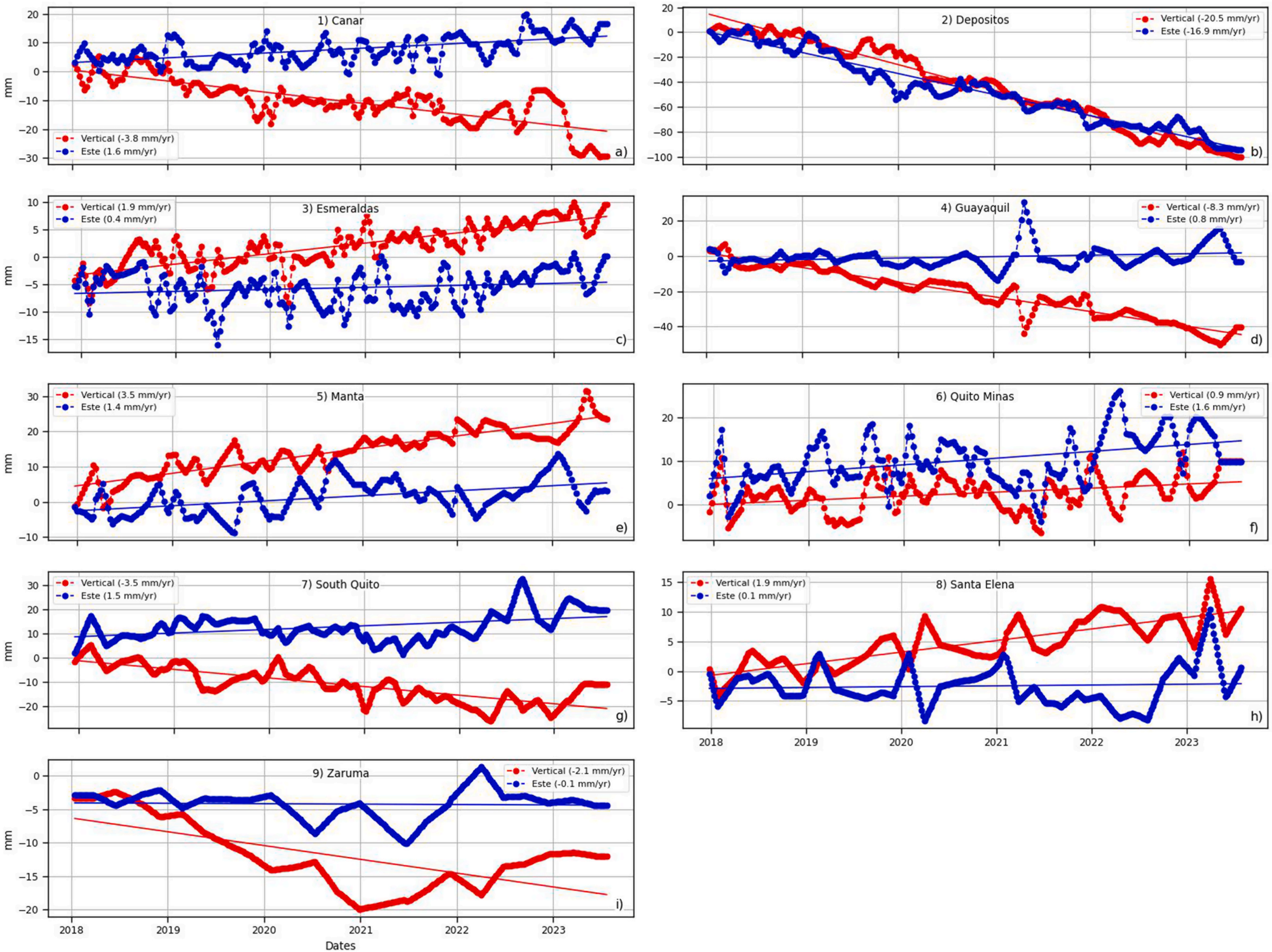

Fig. 7. Interpolated time series of vertical and east-west displacement components for the areas exhibiting anthropogenic and coast signals assuming the methodology define by Wright et al. (2004), with the average linear velocity for horizontal (east-west in red) and vertical (blue) shown. The location points for each time series are shown in Fig. 5. (For interpretation of the references to colour in this figure legend, the reader is referred to the Web version of this article.)

barrier of the water body (Catolica, 2021).

Finally, two signals associated with mining of volcano-sedimentary deposits have been identified. The first is located in the northern part of Quito (Fig. 5k), where material is extracted for construction. This activity likely destabilizes the slopes and has led to land slip behaviour with deformation of −3.6 mm/yr in the vertical component. The second signal is north-northeast of Cuenca (Fig. 5f), where volcanic tuffs, sandstones and shales/mudrocks crop out (Egüez et al., 2017). This region exhibits a subsidence rate of 20.3 mm/yr (Fig. 7b), with a linear velocity in the line of sight (LOS) of −20.6 mm/yr on the descending track (Supplementary Fig. S16b).

3.3. Coast cities deformation

In the coastal zone, the cities of Esmeraldas (Fig. 5o), Manta (Fig. 5q), and Santa Elena (Fig. 5) exhibit good coherence and significant deformation in the horizontal component is observed. Two cities on the Ecuadorian coast, Esmeraldas and Santa Elena, exhibit horizontal eastward velocities of 16 mm/yr and 12 mm/yr, respectively, in our decomposed east-west velocity, which would be associated with the north-eastern movement of the NAS due to the subduction. In addition, the interpolated series of components shows a vertical displacement of 1.9 mm/yr and a horizontal displacement of 0.4 mm/yr for both Esmeraldas and Santa Elena (Fig. 7c–h).

Similarly, the LOS (line-of-sight) time series for Esmeraldas indicates constant linear velocities on two tracks: 1.5 mm/yr on the descending track and 1 mm/yr on the ascending track (Supplementary Fig. S16c). In contrast, for Santa Elena, both tracks exhibit line-of-sight velocities of approximately 1 mm/yr (Supplementary Fig. S16h). These differences are primarily due to the fact that our choice of reference for the time series is a local site, as compared to the reference of decomposed velocity.

3.4. Slip rate and locking depth modeling of the Pallatanga fault section

Our regional derived horizontal (east-west) velocity displays a general east-west gradient in the northern region of the Cosanga-Chingual-Pallatanga-Pisayambo (CCPP), accompanied by significant deformation extending southward, which correlates with the fault system located further south, encompassing the Guamote, Cebada, and Peltetec faults. To analyse this in terms of estimating a fault slip and potentially the depth extent of the locked fault, we model fault-perpendicular profiles based on our estimated east-west velocity field near Pallatanga (indicated by the blue dashed square in Fig. 1a), a segment of the CCPP (Fig. 6). We do this using a simple analytical elastic screw dislocation model (Savage and Burford, 1973). We utilize two dislocation models (as described in Equation (2)) because our map reveals a velocity variation in this region associated with both the main Pallatanga fault and the southern fault trace, which comprises the Guamote, Columbe, Pilaloma, La Moya, Alausi, Cebada, and Peltetec fault segments situated further to the southeast (abbreviations of the labelled faults are presented in Fig. 9).

$$V_{para}(x) = \left(\frac{S_1}{\pi}\right) arctan\left(\frac{x}{d_1}\right) + \left(\frac{S_2}{\pi}\right) arctan\left(\frac{x + C_1}{d_2}\right) + C_2 \tag{2}$$

where V_{para} is the horizontal velocities parallel to the fault, x is the perpendicular distance from the fault, S_1 and d_1 are the slip rate and locking depth of the main CCPP fault, S_2 and d_2 are the slip rate and locking depth of the southern fault, C_1 is an offset in the location of the southern fault relative to the fixed main fault and C_2 is a velocity offset.

We determine the optimal values for each model parameter using a Bayesian affine invariant ensemble Markov Chain Monte Carlo (MCMC) approach defined by (Goodman and Weare, 2010). We adopt a uniform prior distribution for all parameters, with bounds set at $1 \leq S_1 \leq 6$ mm/yr, $0.1 \leq d_1 \leq 15$ km, $1 \leq S_2 \leq 5$ mm/yr, $0.1 \leq d_2 \leq 1$ km, $-16 \leq C_1 \leq -17$ km, and $4 \leq C_2 \leq 7$ mm/yr. Our MCMC sampler employs 200 walkers and iterates for 300,000 steps. We discard the initial 20 % of iterations from each walker as burn-in. To incorporate uncertainties, we assign weights to the velocities using a variance-covariance matrix derived from an exponential covariogram, with parameters set as follows: range = 2.0 km, sill = 0.27 $(mm/yr)^2$, and nugget = 0.055 $(mm/yr)^2$. We estimate these values by fitting an exponential function (Supplementary Fig. S17) with a nugget to the isotropic experimental semi-variogram, as described in Bagnardi and Hooper (2018), focusing on the data coverage in the northeastern region where there is minimal deformation and the noise in the east velocity is representative of the noise we expect in this region.

The fault-parallel velocity profile, calculated from the east-west velocity data within a 120-km-wide swath, reveals additional strain distributed over the southern fault system, wherein the Guamote, Cebada, and Peltetec faults are situated. Additionally, we project the GPS data onto the fault-parallel profiles, demonstrating a reasonable fit with the InSAR data (see Fig. 8). The interseismic modeling, which combines two screw dislocation models, indicates a slip rate of 3.2 ± 0.6 mm/yr with a locking depth of 5.4 ± 4 km for the main fault (CCPP), and a slip rate of 2.7 ± 0.3 mm/yr beneath a locking depth of 0.3 ± 0.2 km for the southern fault trace (SFT). The distance between the secondary fault and the fixed location of the main fault is 16 ± 0.1 km. Supplementary Fig. S18 illustrates the marginal posterior probability (MAP) distributions for each parameter. The MAP solutions and uncertainties for each parameter are provided in Supplementary Table S8.

Additionally, we tested using the interpolated North component from our GNSS and the East component from InSAR (e.g. Wang et al. (2024)) to extract the fault-parallel velocities and model them using Equation (2) (Supplementary Figs. S19 and S20). However, we fixed the locking depth of the first fault at an estimated depth of 14 km, as reported by Jarrin et al. (2023). This approach resulted in a small discrepancy in the estimation of slip related to CCPP, which was 2.2 ± 1.1 mm/yr, lower than our estimate derived solely from the East component (3.1 ± 0.7 mm/yr). In the southern region, we observed a slip rate of 1.7 ± 0.5 mm/yr, compared to 2.7 ± 0.3 mm/yr of our estimate derived solely from the East component. The model is likely underestimating in the near field due to topographically correlated noise in the northwest along the profile, specifically between 2 km and 50 km, where Chimborazo Volcano is located. Additionally, this discrepancy may be attributed to the smooth interpolation of the north component and the assumption of a fixed fault depth.

3.5. Strain rate estimation across Pallatanga-Riobamba area

We estimate the horizontal strain rate field from our InSAR east velocities (V_E) and interpolated GNSS north velocities (V_N) across the Pallatanga area following the method outlined by Ou et al., (2022). First, we apply a sliding median spatial filter (tested over wavelengths of varying 10's km in scale) to our V_E data to suppress noise and non-tectonic short-wavelength signals (e.g. Fang et al., (2022)). We test various window sizes for the median filter window in order to determine the optimal trade-off between noise suppression and signal preservation. Subsequently, we estimate the horizontal gradients of the filtered V_E ($\partial V_E/\partial_x$ and $\partial V_E/\partial y$) and interpolated VN ($\partial V_N/\partial x$ and $\partial V_N/\partial y$). From these four gradient tensors, we derive the horizontal strain-rate tensor, horizontal dilatation rate, maximum shear rate, and the second invariant of the horizontal strain-rate tensor (Figure Supplementary S22). We explored applying several filter window widths (10, 15, 20, 30, 40, 60, and 80 km) (e.g. Watson et al. (2024)). Supplementary Fig. S23 illustrates the effects of using various window sizes and their corresponding profiles. The absence of filtering and the use of smaller window sizes (10–15 km) resulted in random noise dominating between adjacent pixels, which led to elevated strain rates (≥100 nst/yr). This obscured the underlying tectonic signals across the CCPP, as well as in the Latacunga-Pujilí reverse faults to the north of our study area (see

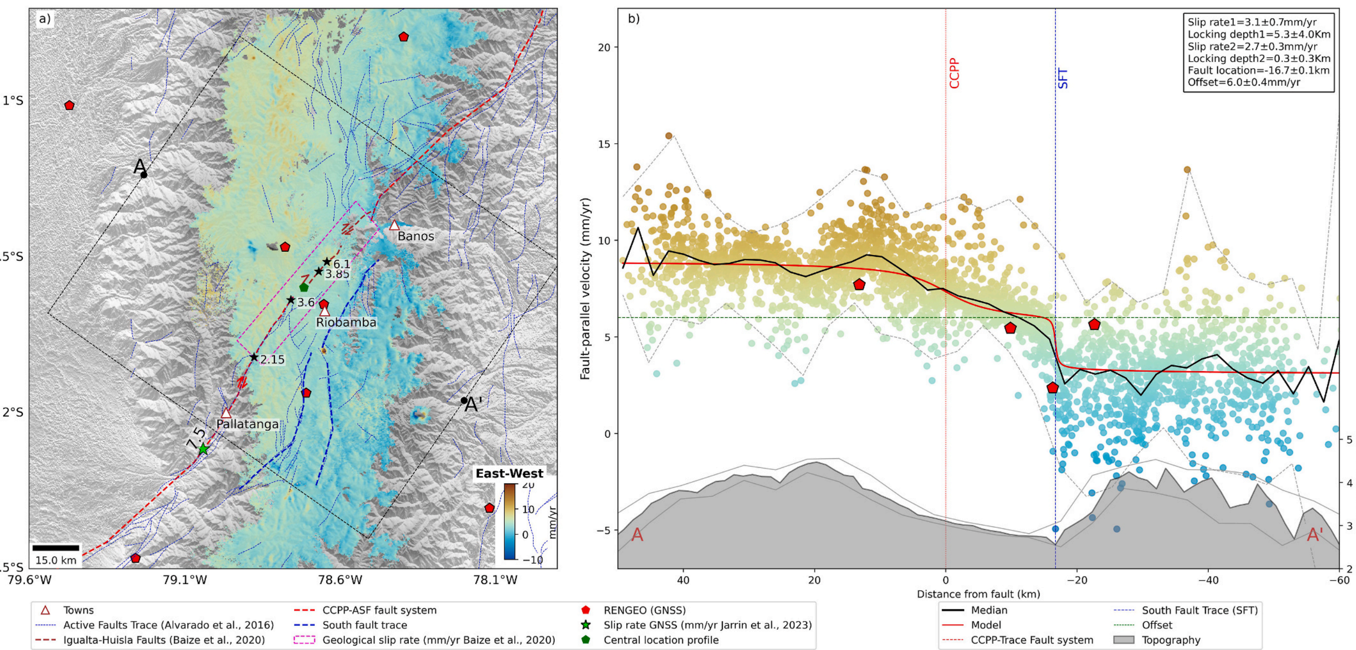

Fig. 8. a) The east-west component of surface velocity between the cities of Pallatanga, Riobamba and Baños, with the black rectangle denoting the extent of the velocity profile A-A′ across the CCPP (red line). These profiles are superimposed onto hill-shaded topography (Copernicus DEM), featuring city locations (marked by white-red triangles), GNSS locations (indicated by red circles), geological slip rates (denoted by black stars), and the slip rate estimated from GNSS (illustrated by the green star). b) Fault-perpendicular profile of fault-parallel velocities (coloured circles) calculated from the east-west InSAR velocities within a 120-km-wide profile, with modeling results (coloured lines) using two screw dislocation models of fault slip beneath a locked elastic lid. GNSS velocities within each profile are depicted by red pentagons. The vertical red line delineates the trace of CCPP faults, while blue dashed lines indicate the fault locations to the southeast. The black line represents the mean value of the data profile, with the red line indicating the model (Equation (2)). (For interpretation of the references to colour in this figure legend, the reader is referred to the Web version of this article.)

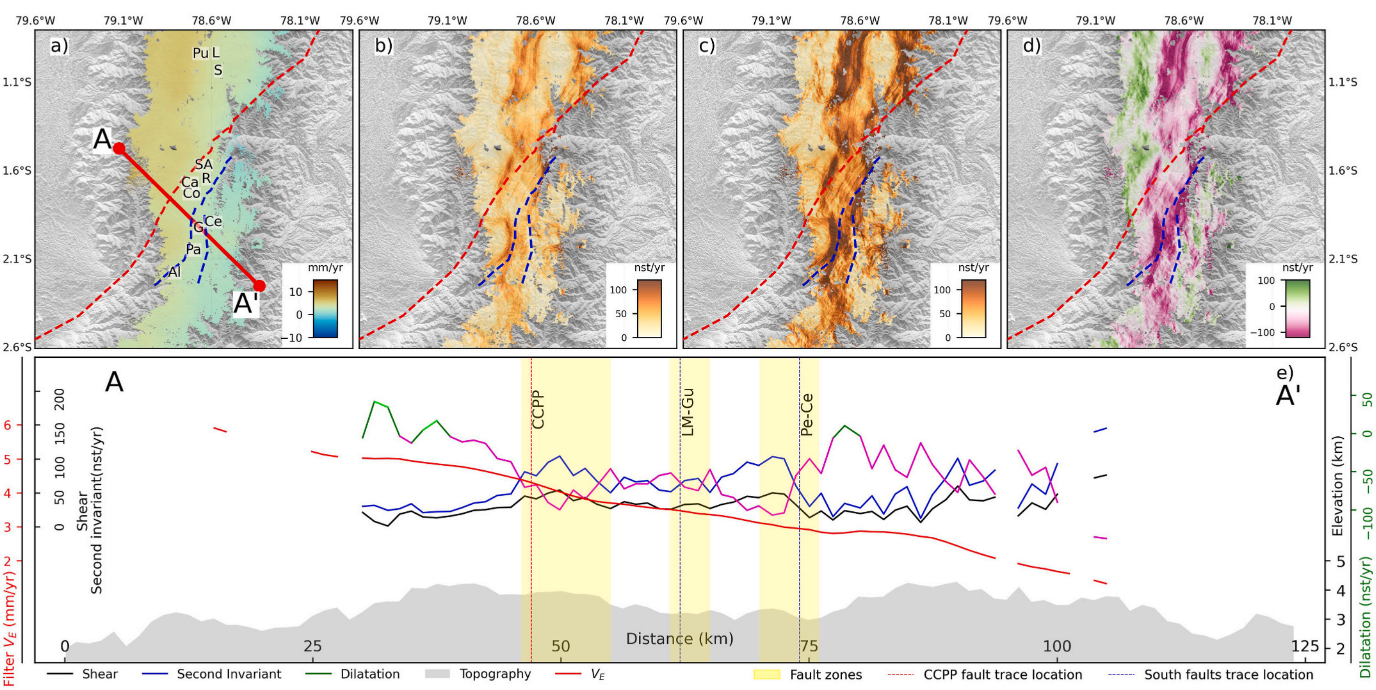

Fig. 9. Interpolated InSAR East velocities (a), smoothed with a 20 km median filter used to calculate (b) the maximum shear strain rate, (c) the second invariant of the strain rate tensor, and (d) the dilatation rate, for the area of CCPP Fault. Negative dilatation indicates contraction. (e) Profiles A-A′ for filtered East velocities, max shear strain rate, second invariant and dilatation rate (profile location shown in a). Abbreviations, Towns: Co=Colta, Ca=Cajabamba, SA=San Andres, R=Riobambam Al=Alausi, G = Guamote, Pa=Palmira, Ce=Cebada, L = Latacunga, Pu=Pujili, S=Salcedo. Faults: CCPP=Cosanga-Chingual-Pallatanga-Pisayambo, Pe-Ce= Peltetec-Cebada, LM-Gu = La Moya-Guamote.

Figure Supplementary S23b, e, h, q). Conversely, window sizes between 40 and 80 km excessively smoothed the eastward component of velocity (Supplementary Figs. S23a,f,g,h), leading to the loss of the localised interseismic signal and impacting the estimation strain rates (≤50 nst/yr) and dilatation, thus resulting in decreased peak magnitudes and increased spatial simplification of the signals (Supplementary Fig. S24). We found that a 20 km filter window (Fig. 9a) yielded optimal results for preserving the interseismic fault signal and reducing noise in our InSAR V_E data.

The strain rate signals identified (Fig. 9) align with the CCPP fault trace (illustrated by the red line in Fig. 9), predominantly concentrated within the vicinity encompassing Cajabamba, San Andres, and Colta. This region exhibits maximum shear strain rates ranging between 50 and 70 nst/yr (Fig. 9b–e). Additionally, significant rates of strain are discernible towards the southeast, coinciding with the southern fault trace extending from Alausi to Palmira (indicated by the blue line in Fig. 9b), with shear rates between 30 and 70 nst/yr (Fig. 9b–e). The manifestation of this signal progressively reduces as it extends southeastward towards the Peltetec-Cebada fault trace, as demonstrated by both the unfiltered (Fig. 8) and filtered east-west velocity profiles. Noteworthy signals also emerge in association with the thrust fault Latacunga-La Victoria system and anticlinal folds (Lavenu et al., 1995b), traversing northward of the CCPP between the cities of Latacunga, Pujili, and Salcedo, with shear rates ranging from 40 to 70 nst/yr. In areas along the fault trace where high shear strain prevails, the dilatation rate demonstrates contraction (Fig. 9d and e).

4. Discussion

We have successfully obtained contemporary surface movements for 19 % (~55, 359 km^2) of the land surface area of Ecuador, with coverage greatest along the inter-Andean valley and some coastal cities. This was

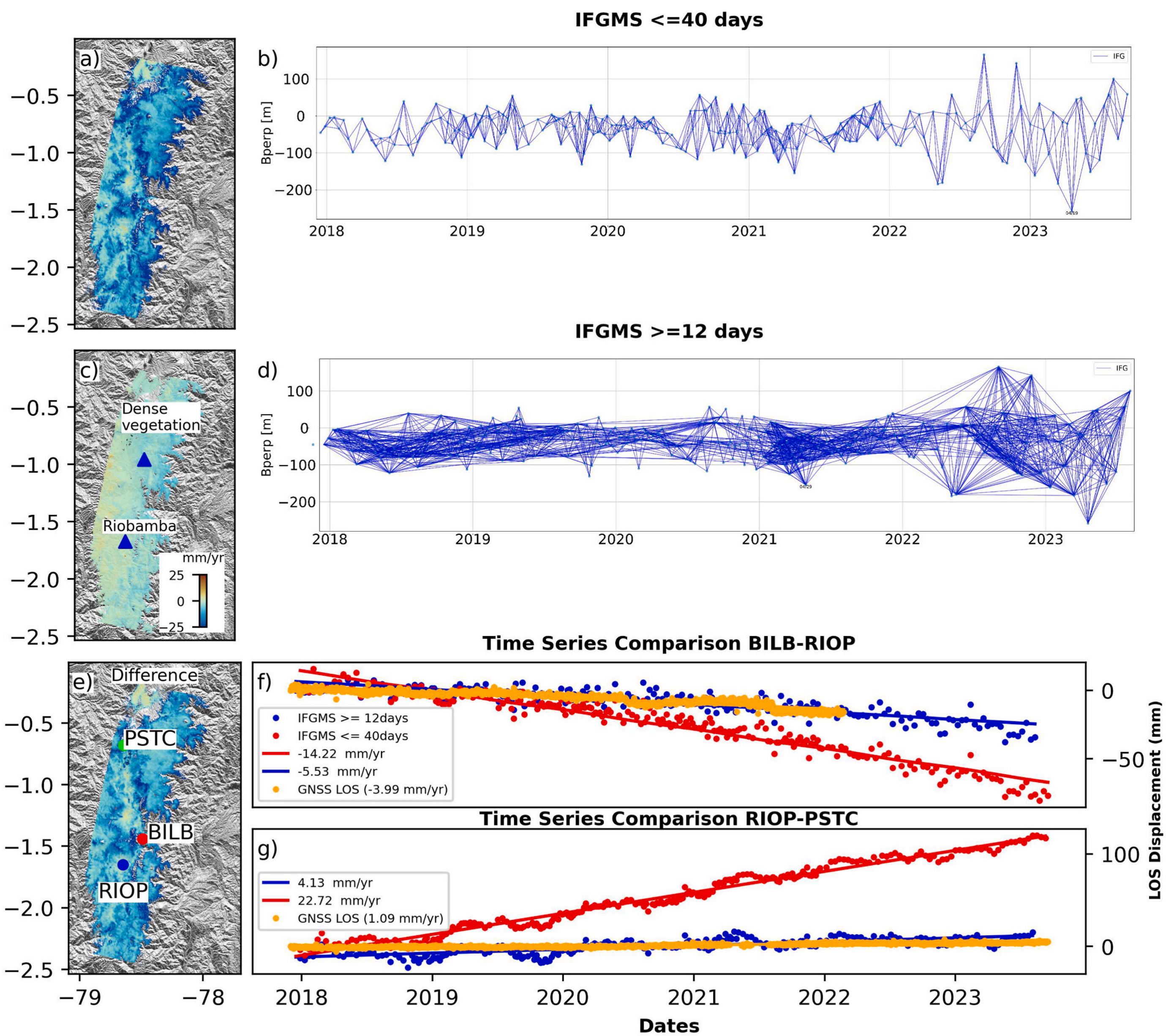

Fig. 10. Velocity field results and interfeogram networks between different combinations of short only and combined short and longer interferograms for a descending frame (142D 09148 131313). (a), (b) ≤ 40 days; (c), (d) ≥ 12 days, (e) Difference between both velocities. (f) Time series comparison between the InSAR from (a),(b) and the projected GNSS-LOS from the points of GNSS station BILB relative to a reference station RIOP, (g) Time series comparison between the InSAR from (a),(c) and the project GNSS-LOS from the points of GNSS station RIOP relative to a reference station PSTC.

a challenging task due to the country's diverse vegetation and the decorrelation it induces in C-band interferometry, thereby affecting data coherence and the atmospheric variations. Through the implementation of a robust network of interferograms, we have been able to discern signals associated with volcanic activity, tectonic activities, and human-induced phenomena such as urban subsidence and mining activities. In terms of tectonics, our analysis has focused on the slip rate and strain rate at a broader scale within the border region between the North Andean block and the South American plate, specifically within the Pallatanga and Riobamba area.

4.1. Time series network strategy

The optimal network and processing strategy should involve utilizing short time-span interferograms in regions like Ecuador to maintain coherence in areas with high decorrelation (e.g. $\leq$ 40 days, Fig. 10b). However, these types of networks introduce systematic effects into our velocity and time series, consistent with the concept of a 'fading signal' as defined by Ansari et al. (2021). Fading signal is a source of error in the phase of InSAR. This signal or bias accumulates in surface velocities derived from short-baseline networks of multi-looked interferograms (De Zan et al., 2015; Ansari et al., 2021; Maghsoudi et al., 2021). Although this error may be small in each interferogram, it has a significant impact over the time series, particularly when the measurement is very small, in the millimetric range. We have observed that this signal intensifies in areas with dense vegetation and specific soil and land cover types (e.g. Purcell et al. (2022) and Daout et al. (2023)). Furthermore, it also manifests in urban areas characterized by good coherence (see Fig. 10a).

Therefore, we propose a region-specific strategy to mitigate these effects, involving: 1) the exclusion of short 6-day interferograms, and 2) integration with longer interferograms (e.g. Purcell et al. (2022), Daout et al. (2023), and Espín Bedón et al., (2024)), considering the strategy of using interferograms of 12 days or longer (Fig. 10c and d). We compare our InSAR time series from track 142D_09148_131313, obtained using this network configuration, with the LOS-GNSS time series, where both exhibit similar deformation patterns and magnitudes (Fig. 10f and g). Using this strategy (Fig. 10c and d), we first compare the GNSS station BILB, referenced to RIOP, and RIOP, referenced to PSTC (Fig. 10e, f, g). The relative velocity between BILB and RIOP decreases from -14.22 mm/year to -5.53 mm/year when the 6-days interferograms are removed, while the relative velocity between RIOP and PSTC changes from 22.72 mm/year to 4.13 mm/year. Additionally, we can discern that in regions characterized by high vegetation cover (see location in Fig. 10c), exemplified by the area situated to the east of the city of Latacunga, where the apparent deformation rate measurement diminishes from -13.9 to -4.2 mm/yr when removing shorter period inteferograms from the network. Similarly, in areas demonstrating robust coherence, such as the city of Riobamba (see location in Fig. 10c), the deformation rate decreases from 3.17 to 0.03 mm/yr.

4.2. Estimation of slip rates and locking depth

In geodetic and geological investigations of the region between Pallatanga and Riobamba, substantial focus has been placed on the fault trace, revealing deformation strike slip rates of 2–6 mm/yr (Winter et al., 1993; Baize et al. 2015, 2020; Harrichhausen et al., 2023). Extending this analysis using InSAR, our study covered a broader area, as depicted within the blue dashed square in Fig. 1a. This extension revealed that slip is not solely confined to the primary fault trace (the boundary of CCPP) but also propagates onto the southeastern segments, where the Guamote, Columbe, Pilaloma, La Moya, Alausi, Cebada, and Peltetec faults are situated. These faults are described as active transcurrent faults by Alvarado et al., (2016); Pratt et al., (2005); Eguez et al., (2003). The zone in question appears to include ancient structures derived from the primary fault system that remain active (Alvarado et al., 2016; Litherland et al., 1993, 1994).

Champenois et al. (2013) employed a simplified model of a locked strike-slip fault to estimate a slip rate of 9 mm/yr with a locking depth of 7 km on the main fault. In contrast, Marconato et al. (2024b) using ALOS data, found a slip rate of 6.3 mm/yr. Moreover, using a decollement-ramp junction model, Marconato et al. (2024a) found a net slip rate of approximately 9 mm/yr. Our adoption of a two-screw dislocation model produced a strike-slip rate of 3.2 mm/yr consistent with the geological range (between 2.15 and 6.1 mm/yr, Baize et al. (2020)) and indicated a locking depth of 5 $\pm$ 4 km, which is notably lower than the 14 $\pm$ 1 km depth reported by Jarrin et al. (2023) for crustal faults in this region, and also less than the seismic depth of 18 km estimated by Beauval et al. (2018). This discrepancy may be due to stress readjustments during the seismic cycle (Smith-Konter et al., 2011), potentially influenced by recent seismic events such as the Riobamba earthquakes of 1797 and 1698 (Beauval et al., 2010; Beauducel et al., 2020). Additionally, the broader distribution of strain observed when considering two parallel faults, as opposed to a single fault, may further explain this variation. Attempting to model such a broad strain pattern with a single fault can result in an overestimation of the locking depth, as the strain becomes less localized and more distributed over depth and along strike. However, this is very similar to the depth estimated by Marconato et al. (2024a), which falls within a range of 7.3 $\pm$ 2.9 km. Alternatively, it could reflect variations in slip distribution within the southeastern fault system. The observed movement of 2.7 mm/yr in this zone contrasts with Eguez et al. (2003) who suggested a movement of less than 1 mm/yr, highlighting an area of uncertainty in current slip rate estimations.

4.3. Patterns of strain rate and tectonic regime

The estimation of geodetic velocity fields provides constraints on strain rates within active fault zones (Elliott et al., 2016), which can be related to seismic hazard assessment aimed at identifying future seismic event occurrences (e.g. Zhao et al. (2022a), Fang et al. (2022), Zhao et al. (2022b), Wright et al. (2023), Hussain et al. (2023), and Maurer and Materna (2023)). As outlined in the preceding section, we estimated the strain rate using the methodology established by Ou et al. (2022), incorporating a median filter into our east velocity data and the interpolated North velocity. Regarding the selection of filter window size, both Ou et al. (2022) and Fang et al. (2022) employed a 60 km window to isolate interseismic strain accumulation along active faults and mitigate short-wavelength noise for velocities ranging from 3 to 15 mm/yr. We selected a window size of 20 km to smooth our eastward velocity, aiming to retain the interseismic fault signals while effectively mitigating short-wavelength noise. This approach is well-suited for interseismic strain over short distances or wavelengths, as it maintains the residual post-seismic signal over long wavelengths before the Pedernales subduction earthquake. Fig. 9c–e illustrates that the maximum peak strain rate, quantified by the second invariant, and is primarily localised within the north-eastern zones along the fault trace, including the CCPP (red dashed line in Fig. 9) and areas to its south (blue dashed line in Fig. 9). These values range between 50 and 100 nst/yr. Additionally, between the two primary fault lines, the values range from 30 to 60 nst/yr. Arcila and Muñoz–Martín (2020) estimated the strain rate (second invariant) for the entire South American region using focal mechanisms and the GPS network until 2017 (Figure Supplementary S25b). For our study area, this estimation indicates a rate ranging between 30 and 80 nst/yr. Similarly, Vaca et al. (2019) estimated a horizontal strain rate 20.8 $\pm$ 7.1 nst/yr north of the city of Riobamba based on data from five GPS stations up to 2014. Additionally, Staller et al. (2018) employed the Delaunay triangulation method on GNSS data from 2008 to 2014, estimating a maximum shear of approximately 100 nst/yr (Figure Supplementary S25c). The integration of InSAR and GNSS strain rates enables more precise localization and accurate depiction of the actual distance over which velocity changes occur, compared to relying solely on GNSS-based strain rate values.

Our results confirm the observations made by Vaca et al. (2019) that most of the deformation is absorbed by the CCPP system and NAS faults. However, Marconato et al. (2024a) report a strain rate exceeding 200 nst/yr in the region. Moreover, higher strain rates observed throughout the Latacunga–Pujili area may capture the broad deformation of anticline folds resulting from shortening due to thrust faults (Lavenu et al., 1995b; Alvarado et al., 2014). The high shear zones do not exhibit major seismic events (but rather events smaller than Mw 3, (Beauval et al., 2013; Beauval et al., 2018), indicating either continuous movement (CCPP major fault trace) or more effective tectonic loading (Zhao et al., 2022a; Melosh et al., 2018), or possibly an incomplete or too-short seismic catalog. Historical earthquakes (Beauval et al., 2018), such as Ambato in 1698 (Mw 7.2) and Riobamba in 1797 (Mw 7.6)

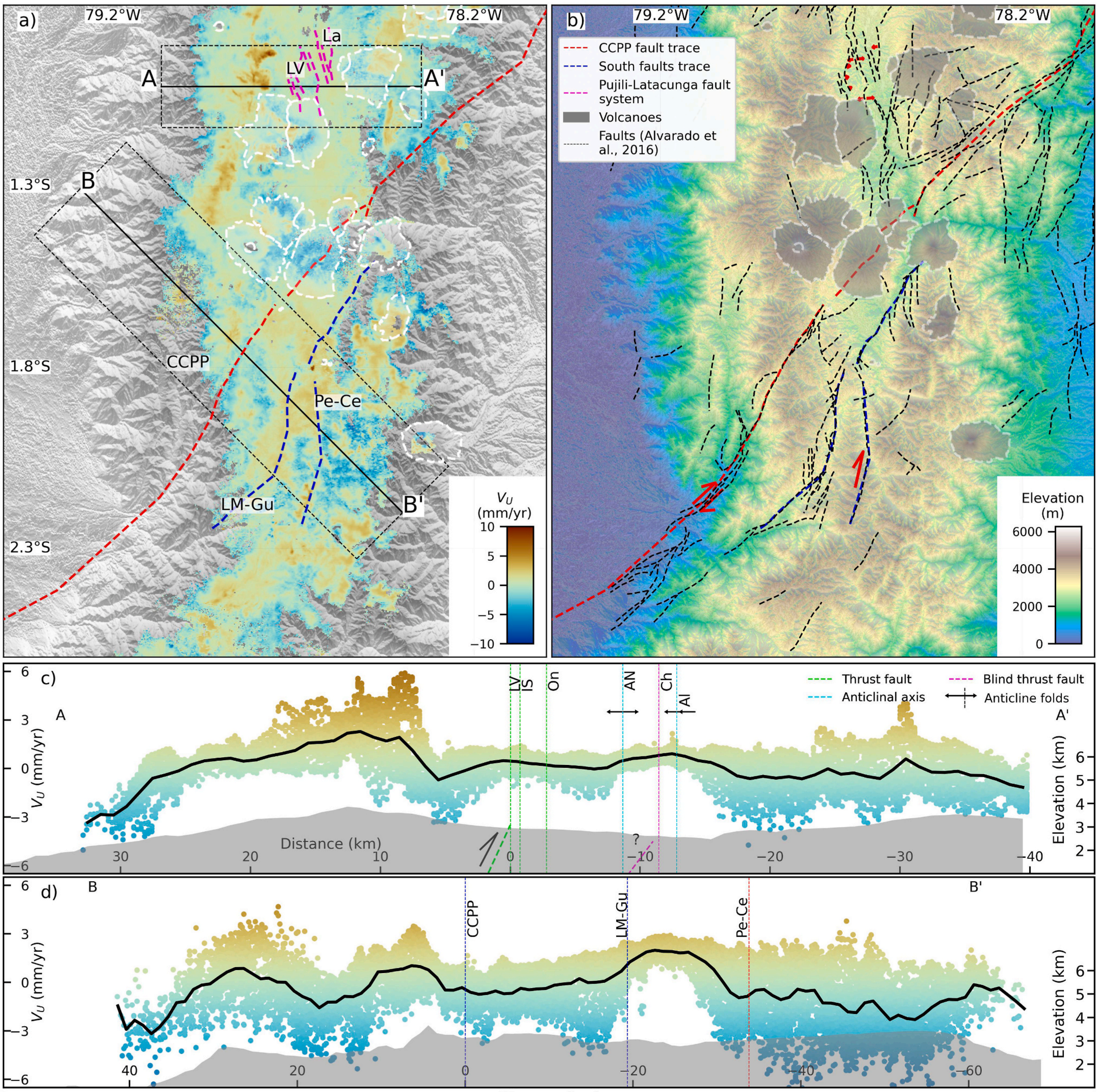

Fig. 11. Interpretations of vertical component of surface velocity in the area between the cities of Pallatanga, Riobamba and Baños (a). See the location in Fig. 5. (b) Digital elevation model (DEM) in meters from Copernicus (European Space AgencySinergise, 2021). (c) A–A′ profile (location in (a)) across Latacunga–Pujili fault system. (d) B–B′ profile (location in (a)) across the main trace CCPP fault system. Red lines show positive deformation and blue lines show subsidence in (c) and (d). Abbreviations: LV: La victoria reverse fault, La: Latacunga reverse fault, CCPP: Chingual–Cosanga–Pallatanga–Puná Fault System, LM-Gu: La Moya Guamote faults, Pe-Ce: Peltec-Cebada dextrals faults, IS: Isinche reverse fault, On: Once de Noviembre reverse fault, AN: Acurios–Nagsiche fold axis, Ch: Chatag reverse blind fault, Al: Alaquez fold axis (trace of the faults from Lavenu et al. (1995b), Eguez et al. (2003), and Alvarado et al. (2014)). In the profiles c and d, the topography is shown in grey shading. (For interpretation of the references to colour in this figure legend, the reader is referred to the Web version of this article.)

(Supplementary Fig. S26), are situated in areas with lower maximum shear strain rates, where locked faults could potentially generate significant seismic events in the future.

Ecuador's tectonic setting is highly influenced by the interaction of the South American Plate and the Nazca Plate. This subduction process drives significant east-west compression across the region, leading to the uplift of the Andes mountains and intense seismic activity (Pennington, 1981; Acosta, 1983; Lavenu et al., 1995a). Focusing on the study area, our dilation estimate shows contraction in most of the area (negative values in Supplementary Fig. S26), following the direction of the fault traces, which would be related to the ENE-WSW shortening estimated by Assumpção et al. (2016) and Arcila and Muñoz–Martín (2020) (Supplementary Fig. S25b), in agreement with negative dilatation estimated by Staller et al. (2018) (Supplementary Fig. S25c).

4.4. Vertical surface displacements

We observe a first-order correlation in the area of the CCPP between vertical motion and topography, primarily focusing on the high elevation areas of the mountain range. However, as discussed in section 2.2, we applied a correction to reduce the atmospheric component associated with topography. Additionally, as detailed in Section 2.4, distinct vertical movements linked to volcanic activity, land subsidence due to specific deposits, and mining activities can be identified (see Fig. 5).

In the profile of Fig. 11d, it is evident that positive vertical deformation aligns with the topography (Fig. 11). Although there are slight traces of reverse movement (Baize et al., 2015), no significant vertical displacement are associated with the faults. However, indications of subsidence, ranging between 1 and 2.7 mm/yr, are noted between the CCPP faults and La Moya-Guamote fault trace, as well as further southeast of the Peltetec–Cebada fault trace. These instances of subsidence likely stem from various factors such as linear ridges, drainage offsets, cumulative scarps, and counterscarps (Baize et al., 2015), indicative of shallow processes predominantly on or near the surface. Moreover, when juxtaposed with the landcover types (Fig. 1b), these areas predominantly correspond to flooded vegetation. This particular terrain type is prone to subsidence due to the satellite signal experiencing deviation upon reflection from both the vegetation and the flooded areas (Lu et al., 2010).

In the northern segment of the Latacunga-La Victoria reverse fault and fold system (see Fig. 11), which is characterized by an east-west compressional regime and a N-S strike (Lavenu et al., 1995b; Fiorini and Tibaldi, 2012), our observations of vertical deformation (depicted in Fig. 11a–c) reveal rates of up to 1.1 ± 0.4 mm/yr. These findings corroborate both geological and geodetic data, which indicate a slight apparent movement ranging from ≤ 1 to 1.4 mm/yr (Lavenu et al., 1995b; Eguez et al., 2003; Alvarado et al., 2014).

Moreover, within the axial region of the Acurios-Nagsiche (AN) fold, we have detected minor subsidence (Fig. 11c), potentially corresponding to the synclinal portion of this structure, attributed to blind thrust faults with shallow westward dip angles (Fiorini and Tibaldi, 2012).

4.5. Integrated analysis of volcanic, anthropogenic, and coastal deformation in Ecuador: implications and strategies

The integration of GNSS and InSAR techniques has provided an unprecedented view of volcanic deformation in Ecuador, revealing critical insights into magmatic processes and surface dynamics. The uplift observed at Sangay and Chiles-Cerro Negro is attributable to the magmatic and hydrothermal proccess, with rates up to 15 mm/yr in the Potrerillos region. The importance of horizontal components at Sangay, especially for capturing volcanic flank movement, underscores the necessity of combining GNSS-InSAR and both ascending and descending look directions. Possible subsidence at Reventador and Tungurahua is dominated by deposit compaction in surface deformation. These findings show the importance of multi-component observations to differentiate between magmatic, tectonic, and depositional influences on deformation patterns.

Anthropogenic deformation, particularly in urban centers, reflects the interplay of geological and human-induced factors. Subsidence in cities like Guayaquil and Cañar is tied to sediment compaction and land use, as seen in the subsidence of -7 to -8.8 mm/yr in Guayaquil's clay deposits. Mining activities, such as those near Zaruma, are a clear driver of localized subsidence, with rates exceeding -3 mm/yr. The application of GNSS-InSAR techniques has enabled precise quantification of such deformation trends, providing a robust foundation for mitigating infrastructure risks. While GNSS alone might overlook many subtle deformations due to its limited spatial coverage, the integration with InSAR captures these through its higher spatial density of measurement points. These observations underscore the value of combining GNSS and InSAR data for sustainable urban planning and hazard assessment in regions prone to anthropogenic impacts.

Coastal cities show both tectonic and anthropogenic deformation signatures. The eastward horizontal movements in Esmeraldas and Santa Elena, with velocities of 16 mm/yr and 12 mm/yr, respectively, align with the north-eastward motion of the NAS plate due to subduction. In addition, the vertical displacement of 2 mm/yr in these regions emphasizes the importance of integrating GNSS data to contextualize coastal dynamics. The uplift at Manta further underscores the role of active tectonics, while the comparison of vertical and horizontal components across coastal sites highlights the relative contributions of natural tectonic processes and anthropogenic influences. These findings suggest that while tectonic activity may dominate deformation patterns, human activities can significantly modulate or amplify these effects, underscoring the importance of precise GNSS-InSAR strategies tailored to monitor deformation in Ecuador's complex coastal settings.

The observed deformation, whether volcanic, anthropogenic, or coastal, underscore the efficacy of GNSS-InSAR integration for mapping dynamic systems. A key implication of this work is the demonstrated importance of decomposed horizontal and vertical components in identifying subtle yet significant deformation signals, such as those seen at Cotopaxi, where the northern GNSS component is the sole indicator of movement (Instituto Geofisico (IG-EPN), 2022). To advance GNSS-InSAR strategies in Ecuador, future studies should prioritise higher temporal resolution and incorporate local GNSS networks to refine deformation models. This approach would not only enhance monitoring capabilities but also support effective mitigation of natural and anthropogenic hazards in this geologically active region.

5. Conclusions

In this study, we use over six years of Sentinel-1 interferograms, spanning seven ascending and eight descending frames, to generate InSAR Line-of-Sight (LOS) velocity maps covering one fifth of Ecuador. These are then integrated with data from the IG-EPN GNSS network to produce velocity components, V_E and V_U, at a resolution of approximately 250 m. We have identified distinct vertical surface displacements associated with volcanic activity, land subsidence due to specific deposits, and the impacts of mining activities at this scale. We employ a fault-parallel velocity model for the CCPP trace fault to constrain fault parameters. By employing a screw dislocation model, we estimate a slip rate of 3.1 ± 0.6 mm/yr for the main fault trace and 2.7 ± 0.3 mm/yr for the southern sub-parallel fault. Analysis of the second-invariant of the horizontal strain-rate tensor indicates that strain is accumulating along these major structures, particularly towards the southeast, and also affecting a thrust fault and fold system in the northern region. Additionally, the observed dilation suggests shortening, aligning with the prevailing east-west compression exerted on these fault systems. The proliferation of satellite data, along with the derivation of high-resolution velocity and strain rate maps, represents a significant advancement in accurately measuring the deformation of active faults. This technological progress enhances our ability to monitor and understand seismic activity across various regions. However, it is worth noting that while these advancements have greatly improved our current capabilities, the increased coverage of the country will require the launch of NISAR. This upcoming satellite mission is expected to provide even more comprehensive data at a suitable wavelength for vegetated areas, allowing for better analysis and monitoring of fault movements on a broader scale. Furthermore, this study contributes to a regional perspective on evaluating the hazards associated with deformation and its potential impacts on both eruptive and seismic activities.

CRediT authorship contribution statement

Pedro Alejandro Espín Bedón: Writing – review & editing, Writing – original draft, Validation, Methodology, Investigation, Formal analysis, Data curation, Conceptualization. **John R. Elliott:** Writing – review & editing, Validation, Supervision, Methodology, Funding acquisition, Conceptualization. **Tim J. Wright:** Writing – review & editing, Validation, Supervision, Funding acquisition, Conceptualization. **Susanna Ebmeier:** Writing – review & editing, Validation, Supervision, Funding acquisition, Conceptualization. **Patricia Mothes:** Writing – review & editing, Supervision, Resources. **Milan Lazecky:** Software, Data curation. **Yasser Maghsoudi:** Software, Data curation. **Jack McGrath:** Validation, Software. **Daniel Andrade:** Supervision.

Data availability statement

The Sentinel-1 InSAR data are copyrighted by the European Space Agency and provided freely through the Copernicus Open Access Hub (https://scihub.copernicus.eu/). Sentinel-1 InSAR data are also freely distributed by the Alaska Satellite Facility (https://asf.alaska.edu/). Processed SAR images, coherence, wrapped interferograms, and unwrapped interferograms used in this work can be found on the COMET-LiCS Sentinel-1 InSAR portal (https://comet.nerc.ac.uk/COMET-LiCS-portal/). The time series of the RENGEO national network can be requested directly from the Instituto Geofísico.

Code availability

The LiCSAR software package can be found at https://github.com/comet-licsar. LiCSBAS software can be found at https://github.com/comet-licsar/LiCSBAS (Morishita et al., 2020; Lazecký et al., 2024). Decompose insar velocities matlab scripts for performing a velocity decomposition in https://github.com/andwatson/decompose_insar_velocities (Watson et al., 2022).

Declaration of competing interest

The authors declare that they have no known competing financial interests or personal relationships that could have appeared to influence the work reported in this paper.

Acknowledgments

LiCSAR contains modified Copernicus Sentinel data (2014–2022) analyzed by COMET. LiCSAR uses JASMIN, the UK's collaborative data analysis environment (http://jasmin.ac.uk). PE is supported by the University of Leeds through International Funding and Research Council Funded. SKE is supported by a NERC Independent Research Fellowship (NE/R015546/1). John Elliott is supported by a Royal Society University Research fellowship (UF150282 & URF211006). COMET is the UK Natural Environment Research Council's Centre for the Observation and Modelling of Earthquakes, Volcanoes and Tectonics, a partnership between UK Universities and the British Geological Survey. Figures were produced using Python version 3.10.4. (Python Software Foundation 2022).

Appendix A. Supplementary data

Supplementary data to this article can be found online at https://doi.org/10.1016/j.jsames.2025.105588.

Data availability

Data will be made available on request.

References

Acosta, Carlos Eduardo, 1983. Geodynamics of Ecuador. In: Geodynamics of the Eastern Pacific Region, Caribbean and Scotia Arcs. American Geophysical Union (AGU), pp. 53–63. https://doi.org/10.1029/GD009p0053.eprint isbn: 9781118670279.

Albino, F., Biggs, J., 2021. Magmatic processes in the East African Rift System: insights from a 2015–2020 sentinel-1 InSAR survey. Geochem. Geophys. Geosystems 22, e2020GC009488. https://doi.org/10.1029/2020GC009488.

Alvarado, Alexandra, 2012. Néotectonique et cinématique de la déformation continentale en Equateur. Francia: Université Grenoble 260.

Alvarado, A., Audin, L., Nocquet, J.M., Lagreulet, S., Segovia, M., Font, Y., Lamarque, G., Yepes, H., Mothes, P., Rolandone, F., Jarrín, P., Quidelleur, X., 2014. Active tectonics in Quito, Ecuador, assessed by geomorphological studies, GPS data, and crustal seismicity. Tectonics 33 (2), 67–83. https://doi.org/10.1002/2012TC003224 issn: 02787407.

Alvarado, A., Audin, L., Nocquet, J.M., Jaillard, E., Mothes, P., Jarrín, P., Segovia, M., Rolandone, F., Cisneros, D., 2016. "Partitioning of oblique convergence in the Northern Andes subduction zone: Migration history and the present-day boundary of the North Andean Sliver in Ecuador: eastern limit of the north andean sliver". en. Tectonics 35 (5), 1048–1065. https://doi.org/10.1002/2016TC004117 issn: 02787407.

Alvarado, Alexandra, Ruiz, Mario, Mothes, Patricia, Yepes, Hugo, Segovia, Mónica, Vaca, Mayra, Ramos, Cristina, Enríquez, Wilson, Ponce, Gabriela, Jarrín, Paul, Aguilar, Jorge, Acero, Wilson, Vaca, Sandro, Singaucho, Juan Carlos, Pacheco, Daniel, Córdova, Andrea, 2018. "Seismic, Volcanic, and Geodetic Networks in Ecuador: Building Capacity for Monitoring and Research". en. Seismol Res. Lett. 89 (2A), 432–439. https://doi.org/10.1785/0220170229 issn: 0895-0695, 1938-2057.

Ansari, H., De Zan, F., Parizzi, A., 2021. Systematic interferometric phase biases and their impact on Earth surface deformation monitoring. In: Proceedings of the 13th European Conference on Synthetic Aperture Radar (EUSAR 2021), pp. 1–6.

Arcila, M., Muñoz–Martín, A., 2020. Integrated perspective of the present–day stress and strain regime in Colombia from analysis of earthquake focal mechanisms and geodetic data. In: Gómez, J., Pinilla–Pachon, A.O. (Eds.), The Geology of Colombia, Volume 4 Quaternary, vol. 38. Servicio Geológico Colombiano, Bogotá, pp. 549–569. https://doi.org/10.32685/pub.esp.38.2019.17. Publicaciones Geológicas Especiales.

Arias-Gallegos, Alejandro, Borque-Arancón, M Jesús, GilCruz, Antonio J., 2023. "Present-Day Crustal Velocity Field in Ecuador from cGPS Position Time Series". en. Sensors 23.6, 3301. https://doi.org/10.3390/s23063301 issn: 1424-8220.

Arnold, D.W.D., Biggs, J., Anderson, K., Vallejo Vargas, S., Wadge, G., Ebmeier, S.K., Naranjo, M.F., Mothes, P., 2017. "Decaying Lava Extrusion Rate at El Reventador Volcano, Ecuador, Measured Using High-Resolution Satellite Radar: decaying lava extrusion at el reventador". en. J. Geophys. Res. Solid Earth 122 (12), 9966–9988. https://doi.org/10.1002/2017JB014580 issn: 21699313.

Assumpção, Marcelo, Dias, Fábio L., Zevallos, Ivan, Naliboff, John B., 2016. Intraplate stress field in South America from earthquake focal mechanisms. J. S. Am. Earth Sci. 71, 278–295. https://doi.org/10.1016/j.jsames.2016.07.005 issn: 0895-9811.

Babaee, Sasan, Amin Khalili, Mohammad, Chirico, Rita, Sorrentino, Anna, Martire, Diego Di, 2024. Spatiotemporal characterization of the subsidence and change detection in Tehran plain (Iran) using InSAR observations and Landsat 8 satellite imagery. Remote Sens. Appl.: Society and Environment 36, 101290. https://doi.org/10.1016/j.rsase.2024.101290 issn: 2352-9385.

Bablon, Mathilde, Quidelleur, Xavier, Samaniego, Pablo, Le Pennec, Jean-Luc, Audin, Laurence, Jomard, Hervé, Baize, Stéphane, Liorzou, Céline, Hidalgo, Silvana, Alvarado, Alexandra, 2019. "Interactions between volcanism and geodynamics in the southern termination of the Ecuadorian arc". en. Tectonophysics 751, 54–72. https://doi.org/10.1016/j.tecto.2018.12.010 issn: 00401951.

Bagnardi, Marco, Hooper, Andrew, 2018. Inversion of Surface Deformation Data for Rapid Estimates of Source Parameters and Uncertainties: A Bayesian Approach. en. Geochem. Geophys. Geosystems 19 (7), 2194–2211. https://doi.org/10.1029/2018GC007585 issn: 1525-2027, 1525-2027.

Baize, Stéphane, Audin, Laurence, Winter, Thierry, Alvarado, Alexandra, Moreno, Luis Pilatasig, Taipe, Mercedes, Reyes, Pedro, Kauffmann, Paul, Yepes, Hugo, 2015. "Paleoseismology and tectonic geomorphology of the Pallatanga fault (Central Ecuador), a major structure of the South-American crust". en. Geomorphology 237, 14–28. https://doi.org/10.1016/j.geomorph.2014.02.030 issn: 0169555X.

Baize, Stéphane, Audin, Laurence, Alvarado, Alexandra, Jomard, Hervé, Bablon, Mathilde, Champenois, Johann, Espin, Pedro, Samaniego, Pablo, Quidelleur, Xavier, Le Pennec, Jean-Luc, 2020. "Active Tectonics and Earthquake Geology Along the Pallatanga Fault, Central Andes of Ecuador". en. Front. Earth Sci. 8, 193. https://doi.org/10.3389/feart.2020.00193 issn: 2296-6463.

Beauducel, François, Peltier, Aline, Villié, Antoine, Suryanto, Wiwit, 2020. "Mechanical Imaging of a Volcano Plumbing System From GNSS Unsupervised Modeling". en.

Geophys. Res. Lett. 47, 17. https://doi.org/10.1029/2020GL089419 issn: 0094-8276, 1944-8007.

Beauval, Céline, Yepes, Hugo, Bakun, William H., Egred, José, Alvarado, Alexandra, Singaucho, Juan-Carlos, 2010. "Locations and magnitudes of historical earthquakes in the Sierra of Ecuador (1587-1996)". en. Geophys. J. Int. https://doi.org/10.1111/j.1365-246X.2010.04569.x issn: 0956540X, 1365246X.

Beauval, Céline, Yepes, Hugo, Palacios, Pablo, Segovia, Monica, Alvarado, Alexandra, Font, Yvonne, Aguilar, Jorge, Troncoso, Liliana, Vaca, Sandro, 2013. "An earthquake catalog for seismic hazard assessment in Ecuador". Bull. Seismol. Soc. Am. 103 (2A), 773–786. https://doi.org/10.1785/0120120270.

Beauval, C., Marinière, J., Yepes, H., Audin, L., Nocquet, J.-M., Alvarado, A., Baize, S., Aguilar, J., Singaucho, J.-C., Jomard, H., 2018. "A New Seismic Hazard Model for Ecuador". en. Bull. Seismol. Soc. Am. 108 (3A), 1443–1464. https://doi.org/10.1785/0120170259 issn: 0037-1106, 1943-3573.

Béjar-Pizarro, Marta, Gómez, José, Staller, Alejandra, Luna, Marco, Pérez-López, Raúl, Monserrat, Oriol, Chunga, Kervin, Lima, Aracely, Galve, Jorge, Díaz, José, Mateos, Rosa, Herrera, Gerardo, 2018. "InSAR-Based Mapping to Support Decision-Making after an Earthquake". en. Remote Sens. 10 (6), 899. https://doi.org/10.3390/rs10060899 issn: 2072-4292.

Bemelmans, M.J.W., de Zeeuw- van Dalfsen, Elske, Poland, Michael P., Johanson, Ingrid A., 2021. Insight into the may 2015 summit inflation event at kilauea volcano, Hawai'i. J. Volcanol. Geoth. Res. 415, 107250. https://doi.org/10.1016/j.jvolgeores.2021.107250 issn: 0377-0273.

Bemelmans, M.J.W., Biggs, J., Poland, M., Wookey, J., Ebmeier, S.K., Diefenbach, A.K., Syahbana, D., 2023. High-resolution InSAR reveals localized pre-eruptive deformation inside the crater of Agung volcano, Indonesia. J. Geophys. Res. Solid Earth 128, e2022JB025669. https://doi.org/10.1029/2022JB025669.

Biggs, Juliet, Pritchard, Matthew E., 2017. Global Volcano monitoring: what does it mean when volcanoes deform? Elements 13 (1), 17–22. https://doi.org/10.2113/gselements.13.1.17.

Biggs, Juliet, Wright, Tim, Zhong, Lu, Parsons, Barry, 2007. "Multiinterferogram method for measuring interseismic deformation: Denali Fault, Alaska". en. Geophys. J. Int. 170 (3), 1165–1179. https://doi.org/10.1111/j.1365-246X.2007.03415.x issn: 1365-246X, 0956-540X.

Biggs, Juliet, Dogru, Fikret, Dagliyar, Ayse, Albino, Fabien, Yip, Stanley, Brown, Sarah, Anantrasirichai, Nantheera, Atıcı, Gökhan, Feb. 15, 2021. Baseline monitoring of volcanic regions with little recent activity: application of Sentinel-1 InSAR to Turkish volcanoes. Journal of Applied Volcanology 10 (1), 2. https://doi.org/10.1186/s13617-021-00102-x issn: 2191-5040.

Blewitt, Geoffrey, Kreemer, Corné, Hammond, William C., Gazeaux, Julien, 2016. "MIDAS robust trend estimator for accurate GPS station velocities without step detection". en. J. Geophys. Res. Solid Earth 121 (3), 2054–2068. https://doi.org/10.1002/2015JB012552 issn: 2169-9313, 2169-9356.

Bourgois, Jacques, Lahuathe, Juan, Vaca, Wilmer, Verdezoto, Patricio, Cornejo, Renan, 2006. Hoja geologica Cañar, Mapa Geologico del Ecuador, Escala 1:50.000, Republica del Ecuador. Instituto Geografico Militar del Ecuador. In: Mapa Geologico del Ecuador 1/50.000 Direccion Nacional de Geologia, 1 map.

Brown, Christopher F., Brumby, Steven P., Guzder-Williams, Brookie, Birch, Tanya, Hyde, Samantha Brooks, Mazzariello, Joseph, Czerwinski, Wanda, Pasquarella, Valerie J., Haertel, Robert, Simon, Ilyushchenko, Schwehr, Kurt, Weisse, Mikaela, Stolle, Fred, Craig, Hanson, Oliver, Guinan, Moore, Rebecca, Tait, Alexander M., 2022. "Dynamic World, Near real-time global 10 m land use land cover mapping". en. Sci. Data 9 (1), 251. https://doi.org/10.1038/s41597-022-01307-4 issn: 2052-4463.

Butcher, S., Bell, A.F., Hernandez, S., Ruiz, M., 2021. "Evolution of Seismicity During a Stalled Episode of Reawakening at Cayambe Volcano, Ecuador". en. Front. Earth Sci. 9, 680865. https://doi.org/10.3389/feart.2021.680865 issn: 2296-6463.

Cao, Yuxi, Li, Peixian, Hao, Dengcheng, Lian, Yong, Wang, Yuanjian, Zhao, Sihai, 2022. "Analysis of the Relationship between Vegetation and Radar Interferometric Coherence". en. Sustainability 14.24, 16471. https://doi.org/10.3390/su142416471 issn: 2071-1050.

Carrillo Bravo, Antonio, Jeremy, Dominguez-Cuesta, María José, Cuevas-Mons, José, 2021. Aplicación de Técnicas SIG y A-DinSAR al análisis de movimientos del terreno en Guayaquil (Ecuador). es. Tech. rep. Ilustre Colegio Oficial de Geólogos. https://doi.org/10.21028/jacb.2021.04.26.

Catolica, Universidad, 2021. ASENTAMIENTOS en el sector de SOLANDA fase DIAGNOSTICO informe HIDROGEOLOGICO. Tech. rep. Universidad Catolica url: https://metrodequito.gob.ec/wp-content/uploads/2021/01/PUCE-INFORME-HIDROLOGIA_SOLANDA_compressed.pdf.

Chalumeau, Caroline, Agurto-Detzel, Hans, Barros, Louis De, Charvis, Philippe, Galve, Audrey, Rietbrock, Andreas, Alvarado, Alexandra, Hernandez, Stephen, Beck, Susan, Font, Yvonne, Hoskins, Mariah C., León-Ríos, Sergio, Meltzer, Anne, Lynner, Colton, Rolandone, Frederique, Nocquet, Jean-Mathieu, Régnier, Marc, Ruiz, Mario, Soto-Cordero, Lillian, Vaca, Sandro, Segovia, Mónica, 2021. "Repeating Earthquakes at the Edge of the Afterslip of the 2016 Ecuadorian M W 7.8 Pedernales Earthquake". en. J. Geophys. Res. Solid Earth 126 (5), 2169–9356. https://doi.org/10.1029/2021JB021746 issn: 2169-9313.

Champenois, Johann, Audin, Laurence, Baize, Stéphane, Nocquet, J.-M., Alvarado, Alexandra, 2013. Interseismic deformations along Ecuador active fault systems: contribution of space-borne SAR Interferometry. In: AGU Spring Meeting Abstracts, T22A–01.

Champenois, J., Baize, S., Vallee, M., Jomard, H., Alvarado, A., Espin, P., Ekström, G., Audin, L., 2017. "Evidences of Surface Rupture Associated With a Low-Magnitude (M w 5.0) Shallow Earthquake in the Ecuadorian Andes: Andean Earthquake Surface Rupture". en. J. Geophys. Res. Solid Earth 122 (10), 8446–8458. https://doi.org/10.1002/2017JB013928 issn: 21699313.

Chen, Y., Yu, S., Tao, Q., Liu, G., Wang, L., Wang, F., 2021. Accuracy verification and correction of D-InSAR and SBAS-InSAR in monitoring mining surface subsidence. Remote Sens. 13.21, 4365. https://doi.org/10.3390/rs13214365.

Chlieh, M., De Chabalier, J.B., Ruegg, J.C., Armijo, R., Dmowska, R., Campos, J., Feigl, K. L., 2004. "Crustal deformation and fault slip during the seismic cycle in the North Chile subduction zone, from GPS and InSAR observations". en. Geophys. J. Int. 158 (2), 695–711. https://doi.org/10.1111/j.1365-246X.2004.02326.x issn: 0956540X, 1365246X.

Chlieh, M., Mothes, P.A., Nocquet, J.-M., Jarrin, P., Charvis, P., Cisneros, D., Font, Y., Collot, J.-Y., Villegas-Lanza, J.-C., Rolandone, F., Vallée, M., Regnier, M., Segovia, M., Martin, X., Yepes, H., 2014. "Distribution of discrete seismic asperities and aseismic slip along the Ecuadorian megathrust". en. Earth Planet Sci. Lett. 400, 292–301. https://doi.org/10.1016/j.epsl.2014.05.027 issn: 0012821X.

Choy, George L., Kirby, Stephen H., 2004. "Apparent stress, fault maturity and seismic hazard for normal-fault earthquakes at subduction zones". en. Geophys. J. Int. 159 (3), 991–1012. https://doi.org/10.1111/j.1365-246X.2004.02449.x issn: 0956540X, 1365246X.

Cisneros Medina, A.L., 2017. "Morfo-tectónica de la Península de Manta e Isla de La Plata y su relación con los procesos de subducción". Bachelor's thesis. Quito: Escuela Politécnica Nacional (EPN) url: http://bibdigital.epn.edu.ec/handle/15000/17203.

Cuervas-Mons, José, Domínguez-Cuesta, María José, Carrillo, Jerymy Antonio, 2021. Análisis de movimientos del terreno en Guayaquil (Ecuador) mediante G-POD (A-DInSAR). es. Geogaceta 69, 47–50. https://doi.org/10.55407/geogaceta102382 issn: 2173-6545, 0213-683X.

Daout, S., Jolivet, R., Lasserre, C., Doin, M.-P., Barbot, S., Tapponnier, P., Peltzer, G., Socquet, A., Sun, J., 2016. "Along-strike variations of the partitioning of convergence across the Haiyuan fault system detected by InSAR". en. Geophys. J. Int. 205 (1), 536–547. https://doi.org/10.1093/gji/ggw028 issn: 0956-540X, 1365-246X.

Daout, Simon, D'Agostino, Nicola, Pathier, Erwan, Socquet, Anne, Lavé, Jérome, Doin, Marie-Pierre, Riesner, Magali, Benedetti, Lucilla, 2023. "Along-strike variations of strain partitioning within the Apennines determined from large-scale multi-temporal InSAR analysis". en. Tectonophysics, 230076. https://doi.org/10.1016/j.tecto.2023.230076 issn: 00401951.

Daout, Simon, Sudhaus, Henriette, Kausch, Thore, Steinberg, Andreas, Dini, Benedetta, 2019. "Interseismic and Postseismic Shallow Creep of the North Qaidam Thrust Faults Detected with a Multitemporal InSAR Analysis". en. J. Geophys. Res. Solid Earth 124 (7), 7259–7279 issn: 2169-9313, 2169-9356. doi: 10.1029/2019JB017692. url. https://agupubs.onlinelibrary.wiley.com/doi/10.1029/2019JB017692.

De Zan, F., Zonno, M., López-Dekker, P., 2015. Phase inconsistencies and multiple scattering in SAR interferometry. IEEE Trans. Geosci. Rem. Sens. 53 (12), 6608–6616. https://doi.org/10.1109/TGRS.2015.2444431.

Declercq, P.-Y., Dusar, M., Pirard, E., Verbeurgt, J., Choopani, A., Devleeschouwer, X., 2023. Post mining ground deformations transition related to coal mines closure in the campine coal basin, Belgium, evidenced by three decades of MT-InSAR data. Remote Sens. 15 (3), 725. https://doi.org/10.3390/rs15030725.

Dodds, N., Daout, S., Walker, R.T., Begenjev, G., Bezmenov, Y., Mirzin, R., Parsons, B., 2022. "Interseismic deformation and strain-partitioning along the Main Köpetdag Fault, Turkmenistan, with Sentinel-1 InSAR time series". en. Geophys. J. Int. 230 (3), 1612–1629. https://doi.org/10.1093/gji/ggac139 issn: 0956-540X, 1365-246X.

Dogru, Fikret, Albino, Fabien, Biggs, Juliet, 2023. "Weather model based atmospheric corrections of Sentinel-1 InSAR deformation data at Turkish volcanoes". en. Geophys. J. Int. 234 (1), 280–296. https://doi.org/10.1093/gji/ggad070 issn: 0956-540X, 1365-246X. https://academic.oup.com/gji/article/234/1/280/7040570.

Ebmeier, Susanna K., Elliott, John R., Nocquet, Jean-Mathieu, Biggs, Juliet, Mothes, Patricia, Jarrín, Paúl, Yépez, Marco, Aguaiza, Santiago, Paul, Lundgren, Samsonov, Sergey V., 2016. "Shallow earthquake inhibits unrest near Chiles–Cerro Negro volcanoes, Ecuador–Colombian border". en. Earth Planet Sci. Lett. 450, 283–291. https://doi.org/10.1016/j.epsl.2016.06.046 issn: 0012821X.

Efron, B., Tibshirani, R., 1986. Bootstrap methods for standard errors, confidence intervals, and other measures of statistical accuracy. Stat. Sci. 1 (1), 54–75. https://doi.org/10.1214/ss/1177013815.

Eguez, Arturo, Alvarado, Alexandra, Hugo, Yepes, Machette, Michael N., Costa, Carlos, Dart, Richard L., 2003. Database and map of quaternary faults and folds of Ecuador and its offshore regions. A project of the international lithosphere program task group II-2, major active faults of the world. https://pubs.usgs.gov/of/2003/ofr-03-289/ofr-03-289.html.

Egüez, A., Gaona, Miguel, Albán, Andrea, 2017. Mapa geológico de la República del Ecuador. In: Instituto de Investigación Geológico y En-ergético, Ecuador. It includes a 1.1,000,000.

Elliott, J.R., 2020. Earth observation for the assessment of earthquake hazard, risk and disaster management. Surv. Geophys. 41, 1323–1354. https://doi.org/10.1007/s10712-020-09606-4.

Elliott, J.R., Walters, R.J., Wright, T.J., 2016. The role of space-based observation in understanding and responding to active tectonics and earthquakes. Nat. Commun. 7 (1), 13844. https://doi.org/10.1038/ncomms13844 issn: 2041-1723.

Espín Bedón, P.A., Audin, L., Doin, M.-P., Pinel, V., Pathier, E., Mothes, P., García, A., Samaniego, P., Pacheco, D., 2022. "Unrest at Cayambe Volcano revealed by SAR imagery and seismic activity after the Pedernales subduction earthquake, Ecuador (2016)". en, vol.428. Journal of Vol- canology and Geothermal Research, 107577. https://doi.org/10.1016/j.jvolgeores.2022.107577 issn: 03770273.

Espín, P.A., Audin, L., Doin, M.-P., Pathier, E., Alvarado, A., Thollard, F., Laurent, C., Mariniere, J., Mothes, P., Segovia, M., Vaca, S., Beauval, C., 2018. In: "Deformation monitoring from Synthetic Aperture Radar Interferometry (INSAR) Sentinel data in

Quito, Ecuador". en.. 8th International Symposium on Andean Geodynamics (ISAG), Quito, Ecuador.
Espín Bedón, P.A., Ebmeier, S.K., Elliott, J.R., Wright, T.J., Mothes, P.A., Cayol, V., Magh- soudi, Y., Lazecký, M., Andrade, D., 2024. Co-eruptive, endogenous edifice growth, uplift during 4 years of eruption at Sangay Volcano, Ecuador. In. Journal of Volcanology and Geothermal Research. ISSN: 0377-0273 454, 108147. https://doi.org/10.1016/j.jvolgeores. 2024.108147.
European Space Agency, Sinergise, 2021. Copernicus global digital elevation model. Distributed by OpenTopography. https://doi.org/10.5069/G9028PQB. https://portal.opentopography.org/raster?opentopoID=OTSDEM.032021.4326.3.
Fang, Jin, Qi, Ou, Wright, Tim J., Okuwaki, Ryo, Amey, Ruth M.J., Craig, Tim J., Elliott, John R., Hooper, Andy, Lazecký, Milan, Maghsoudi, Yasser, 2022. "Earthquake Cycle Deformation Associated With the 2021 M W 7.4 Maduo (Eastern Tibet) Earthquake: An Intrablock Rupture Event on a Slow-Slipping Fault From Sentinel-1 InSAR and Teleseismic Data". en. J. Geophys. Res. Solid Earth 127 (11), e2022JB024268. https://doi.org/10.1029/2022JB024268 issn: 2169-9313, 2169-9356.
Fialko, Y., 2006. Interseismic strain accumulation and the earthquake potential on the southern San Andreas fault system. Nature 441 7096, 968–971. https://doi.org/10.1038/nature04797.
Fiorini and Tibaldi, 2012. Quaternary tectonics in the central interandean valley, Ecuador: fault-propagation folds, transfer faults and the Cotopaxi volcano. In: Global and Planetary Change 90-91. Coupled Deep Earth and Surface Processes in System Earth: Monitoring, Reconstruction and Process Modeling, pp. 87–103. https://doi.org/10.1016/j.gloplacha.2011.06.002 issn: 0921-8181.
Geological Survey, U.S., 2023. Earthquake lists, maps, and statistics. url:https://www.usgs.gov/natural-hazards/earthquake-hazards/lists-maps-and-statistics. .
Gómez Cruz, Y., 2020. Modelo analítico de la deformación del complejo volcánico Chiles-Cerro Negro observada mediante imágenes interferométricas de radar de apertura sintética (InSAR). MA thesis. Universidad de los Andes url: http://hdl.handle.net/1992/51282.
Goodman, Jonathan, Weare, Jonathan, 2010. Ensemble samplers with affine invariance. Commun. Appl. Math. Comput. Sci. 5, 65–80.
Grandin, R., Doin, M.-P., Bollinger, L., Pinel-Puyssegur, B., Ducret, G., Jolivet, R., Sapkota, S.N., 2012. "Long-term growth of the Himalaya inferred from interseismic InSAR measurement". en. Geology 40.12, 1059–1062. https://doi.org/10.1130/G33154.1 issn: 0091-7613, 1943-2682.
Hall, M.L., Samaniego, P., Le Pennec, J.L., Johnson, J.B., 2008. Ecuadorian Andes volcanism: a review of Late Pliocene to present activity. J. Volcanol. Geoth. Res. 176 (1), 1–6. https://doi.org/10.1016/j.jvolgeores.2008.06.012.
Hall, M.L., Steele, Alexander L., Bernard, Benjamin, Mothes, Patricia A., Vallejo, Silvia X., Douillet, Guilhem A., Ramón, Patricio A., Aguaiza, Santiago X., Ruiz, Mario C., 2015. Sequential plug formation, disintegration by Vulcanian explosions, and the generation of granular Pyroclastic Density Currents at Tungurahua volcano (2013–2014), Ecuador. J. Volcanol. Geoth. Res. 306, 90–103.
Harrichhausen, Nicolas, Audin, Laurence, Baize, Stéphane, Johnson, Kendra L., Beauval, Céline, Jarrin, Paul, Marconato, Léo, Rolandone, Frédérique, Jomard, Hervé, Nocquet, Jean-Mathieu, Alvarado, Alexandra, Mothes, Patricia A., 2023. "Fault Source Models Show Slip Rates Measured across the Width of the Entire Fault Zone Best Represent the Observed Seismicity of the Pallatanga–Puna Fault, Ecuador". en. Seismol Res. Lett. 1938–2057. https://doi.org/10.1785/0220230217 issn: 0895-0695.
Herring, Thomas A., Melbourne, Timothy I., Murray, Mark H., Floyd, Michael A., Szeliga, Walter M., King, Robert W., Phillips, David A., Puskas, Christine M., Santillan, Marcelo, Wang, Lei, 2016. "Plate Boundary Observatory and related networks: GPS data analysis methods and geodetic products". en. Rev. Geophys. 54 (4), 759–808. https://doi.org/10.1002/2016RG000529 issn: 8755-1209, 1944-9208.
Hidalgo, Silvana, Vasconez, Francisco Javier, Battaglia, Jean, Bernard, Benjamin, Espín, Pedro, Valade, Sébastien, Naranjo, María-Fernanda, Campion, Robin, Salgado, Josué, Córdova, Marco, Almeida, Marco, Hernández, Stephen, Pino, Gerardo, Gaunt, Elizabeth, Bell, Andrew, Mothes, Patricia, Ruiz, Mario, 2022. "Sangay volcano (Ecuador): the opening of two new vents, a drumbeat seismic sequence and a new lava flow in late 2021". en. Volcanica 5 (2), 295–311. https://doi.org/10.30909/vol.05.02.295311 issn: 2610-3540.
Hofmann-Wellenhof, Bernhard, Lichtenegger, Herbert, Wasle, Elmar, 2007. GNSS–global Navigation Satellite Systems: GPS, GLONASS, Galileo, and More. Springer Science & Business Media.
Hooper, Andrew, Bekaert, David, Spaans, Karsten, Arıkan, Mahmut, 2012. "Recent advances in SAR interferometry time series analysis for measuring crustal deformation". en. Tectonophysics 514–517, 1–13. https://doi.org/10.1016/j.tecto.2011.10.013 issn: 00401951.
Hooper, A., et al., 2020. Exploiting InSAR on a large scale for tectonics and volcano monitoring. In: 2020 IEEE International Geoscience and Remote Sensing Symposium. IGARSS, Waikoloa, HI, USA, pp. 6857–6858. https://doi.org/10.1109/IGARSS39084.2020.9323491.
Huntington, K.W., Klepeis, 2017. Challenges and opportunities for research in tectonics: understanding deformation and the processes that link Earth systems, from geologic time to human time. In: A community vision document submitted to the U.S. National Science Foundation." en. University of Washington. Publisher. https://doi.org/10.6069/H52R3PQ5 [object Object].
Hussain, Ekbal, Hooper, Andrew, Wright, Tim J., Walters, Richard J., Bekaert, David P. S., 2016. "Interseismic strain accumulation across the central North Anatolian Fault from iteratively unwrapped InSAR measurements: INTERSEISMIC CENTRAL NAF". en. J. Geophys. Res. Solid Earth 121 (12), 9000–9019. https://doi.org/10.1002/2016JB013108 issn: 21699313.
Hussain, M.A., Chen, Z., Zheng, Y., Shoaib, M., Ma, J., Ahmad, I., Asghar, A., Khan, J., 2022. PS-InSAR based monitoring of land subsidence by groundwater extraction for lahore metropolitan city, Pakistan. Remote Sens. 14.16, 3950. https://doi.org/10.3390/rs14163950, 10.3390/rs14163950.
Hussain, E., Gunawan, E., Hanifa, N.R., Zahro, Q., 2023. The seismic hazard from the Lembang Fault, Indonesia, derived from InSAR and GNSS data. Nat. Hazards Earth Syst. Sci. 23 (10), 3185–3197. https://doi.org/10.5194/nhess-23-3185-2023.
Instituto Geofisico (IG-EPN), 2020. Special report 1th Reventador volcano. Tech. rep. Instituto Geofisico (IG-EPN). https://www.igepn.edu.ec/servicios/busqueda-informes.
Instituto Geofísico (IG-EPN), 2024. Red de Observatorios Vulcanológicos (ROVIG). url: https://www.igepn.edu.ec/red-de-observatorios-vulcanologicos-rovig.
Instituto Geofisico(IG-EPN), 2022. Informe volcánico especial Cotopaxi No 2022-004. Tech. rep 2. url https://www.igepn.edu.ec/servicios/noticias/1990-informe-volcanico-especial-cotopaxi-no-2022-004.
Jácome, Cando, Marcelo, Martinez-Graña, A.M., Valdés, V., 2020. "Detection of Terrain Deformations Using InSAR Techniques in Relation to Results on Terrain Subsidence (Ciudad de Zaruma, Ecuador)". en. Remote Sens. 12 (10), 1598. https://doi.org/10.3390/rs12101598 issn: 2072-4292.
Jarrin, Paúl, 2021. Cinématique actuelle dans les Andes du Nord par GPS. 2021SORUS334. PhD thesis. http://www.theses.fr/2021SORUS334/document.
Jarrin, P., Nocquet, J.-M., Rolandone, F., Mora-Páez, H., Mothes, P., Cisneros, D., 2022. "Current motion and deformation of the Nazca Plate: new constraints from GPS measurements". en. Geophys. J. Int. 232 (2), 842–863. https://doi.org/10.1093/gji/ggac353 issn: 0956-540X, 1365-246X.
Jarrin, P., Nocquet, J.-M., Rolandone, F., Audin, L., Mora-Páez, H., Alvarado, A., Mothes, P., Audemard, F., Villegas-Lanza, J.C., Cisneros, D., 2023. "Continental block motion in the Northern Andes from GPS measurements". en. Geophys. J. Int. 235 (2), 1434–1464. https://doi.org/10.1093/gji/ggad294 issn: 0956- 540X, 1365-246X.
Jolivet, R., Lasserre, C., Doin, M.-P., Peltzer, G., Avouac, J.-P., Sun, J., Dailu, R., 2013. Spatio-temporal evolution of aseismic slip along the Haiyuan fault, China: implications for fault frictional properties. Earth Planet Sci. Lett. 377–378, 23–33. https://doi.org/10.1016/j.epsl.2013.07.020 issn: 0012-821X. https://www.sciencedirect.com/science/article/pii/S0012821X13003956.
Kanamori, Hiroo, McNally, Karen C., 1982. Variable rupture mode of the subduction zone along the Ecuador-Colombia coast. Bull. Seismol. Soc. Am. 72 (4), 1241–1253. https://doi.org/10.1785/BSSA0720041241 issn:0037-1106. https://pubs.geoscienceworld.org/ssa/bssa/article-pdf/72/4/1241/5330551/bssa0720041241.pdf.
Kennan, Lorcan, 2000. In: "Large-scale geomorphology in the central Andes of Peru and Bolivia: Relation to tectonic, magmatic and climatic processes". en. Wiley, pp. 167–192. https://doi.org/10.1016/B978-0-12-385938-9.00003-1.
Krüger, G., Springer, R., Lechner, W., 1994. Global navigation satellite systems (GNSS). Comput. Electron. Agric. 11 (1), 3–21.
Kundu, Bhaskar, Yadav, Rajeev Kumar, Rolandürgmann, Wang, Kang, Panda, Dibyashakti, Gahalaut, Vineet K., 2020. Triggering relationships between magmatic and faulting processes in the May 2018 eruptive sequence at Kılauea volcano, Hawaii. Geophys. J. Int. 222 (1), 461–473. https://doi.org/10.1093/gji/ggaa178.
LaFemina, Peter C., 2015. "Plate Tectonics and Volcanism". en. In: The Encyclopedia of Volcanoes. Elsevier, pp. 65–92. https://doi.org/10.1016/B978-0-12-385938-9.00003-1 isbn: 978-0-12-385938-9.
Lavenu, Alain, Noblet, Christophe, Winter, Thierry, 1995a. Neogene ongoing tectonics in the Southern Ecuadorian Andes: analysis of the evolution of the stress field. J. Struct. Geol. 17 (1), 47–58. https://doi.org/10.1016/0191-8141(94)E0027-V issn: 0191-8141.
Lavenu, Alain, Winter, Thierry, Dávila, Francisco, 1995b. "A Pliocene-Quaternary compressional basin in the Interandean Depression, Central Ecuador". en. Geophys. J. Int. 121 (1), 279–300. https://doi.org/10.1111/j.1365-246X.1995.tb03527.x issn: 0956540X, 1365246X.
Lazecký, Milan, Spaans, Karsten, González, Pablo J., Maghsoudi, Yasser, Morishita, Yu, Albino, Fabien, Elliott, John, Greenall, Nicholas, Hatton, Emma, Hooper, Andrew, Juncu, Daniel, McDougall, Alistair, Walters, Richard J., Scott Watson, C., Weiss, Jonathan R., Wright, Tim J., 2020. "LiCSAR: An Automatic InSAR Tool for Measuring and Monitoring Tectonic and Volcanic Activity". en. Remote Sens. 12 (15), 2430. https://doi.org/10.3390/rs12152430 issn: 2072-4292.
Lazecký, Milan, Qi, Ou, Lin, Shen, McGrath, Jack, Payne, Jessica, Espín, Pedro, Hooper, Andy, Wright, Tim, 2024. Strategies for improving and correcting unwrapped interferograms implemented in LiCSBAS. In: Procedia Computer Science 239. CENTERIS – International Conference on ENTERprise Information Systems/ProjMAN - International Conference on Project MANagement/HCist - International Conference on Health and Social Care Information Systems and Technologies 2023, pp. 2408–2412. https://doi.org/10.1016/j.procs.2024.06.435 issn: 1877-0509.
Litherland, M., Aspden, J., Jemielita, R., 1994. The Metamorphic Belt Sof Ecuador, vol. 11. Overseas Memoir of the British Geological Survey, Nottingham, England, p. 147.
Litherland, M., Aspden, J.A., Egüez, Arturo, 1993. The geotectonic evolution of Ecuador in the phanerozoic.
Liu, F., Elliott, J.R., Craig, T.J., Hooper, A., Wright, T.J., 2021. "Improving the Resolving Power of InSAR for Earthquakes Using Time Series: A Case Study in Iran". en. Geophys. Res. Lett. 48, 14. https://doi.org/10.1029/2021GL093043 issn: 0094-8276, 1944-8007.
Lu, Zhong, Zhang, Jixian, Zhang, Yonghong, Daniel, Dzurisin, 2010. Monitoring and characterizing natural hazards with satellite InSAR imagery. Spatial Sci. 16 (1), 55–66. https://doi.org/10.1080/19475681003700914, 10.1080/19475681003700914.eprint.

Lundgren, P., Bato, M.G., 2021. InSAR applied to volcano hazards. In: 2021 IEEE International Geoscience and Remote Sensing Symposium. IGARSS, Brussels, Belgium, pp. 918–921. https://doi.org/10.1109/IGARSS47720.2021.9553798.
Maghsoudi, Yasser, Lazecky, Milan, Ansari, Homa, Hooper, Andrew J., Wright, Tim J., 2021. "Investigation of the Phase Bias in the Short Term Interferograms". en. In: 2021 IEEE International Geoscience and Remote Sensing Symposium IGARSS. IEEE, Brussels, Belgium, pp. 3380–3383. https://doi.org/10.1109/IGARSS47720.2021.9553631 isbn: 978-1-66540-369-6.
Marconato, L., Audin, L., Doin, M.-P., Nocquet, J.-M., Jarrin, P., Rolandone, F., Harrichhausen, N., Mothes, P., Mora-Páez, H., Cisneros, D., 2024a. Internal deformation of the North andean sliver in Ecuador-southern Colombia observed by InSAR. Geophys. J. Int. https://doi.org/10.1093/gji/ggae338, 10.1093/gji/ggae338.
Marconato, L., Doin, M.P., Audin, L., Pathier, E., 2024b. Ionospheric compensation in L-band InSAR time-series: performance evaluation for slow deformation contexts in equatorial regions. Science of Remote Sensing 9, 100113. https://doi.org/10.1016/j.srs.2023.100113 issn: 2666-0172.
Mariniere, J., Nocquet, J.-M., Beauval, C., Champenois, J., Audin, L., Alvarado, A., Baize, S., Socquet, A., 2020. "Geodetic evidence for shallow creep along the Quito fault, Ecuador". en. Geophys. J. Int. 220 (3), 2039–2055. https://doi.org/10.1093/gji/ggz564 issn: 0956-540X, 1365-246X.
Maubant, L., Pathier, E., Daout, S., Radiguet, M., Doin, M.-P., Kazachkina, E., et al., 2020. Independent component analysis and parametric approach for source separation in InSAR time series at regional scale: application to the 2017–2018 slow slip event in Guerrero (Mexico). J. Geophys. Res. Solid Earth 125, e2019JB018187. https://doi.org/10.1029/2019JB018187.
Maubant, Louise, Radiguet, Mathilde, Pathier, Erwan, Doin, Marie-Pierre, Cotte, Nathalie, Kazachkina, Ekaterina, Kostoglodov, Vladimir, 2022. Interseismic coupling along the Mexican subduction zone seen by InSAR and GNSS. Earth Planet Sci. Lett. 586, 117534. https://doi.org/10.1016/j.epsl.2022.117534 issn:0012-821X.
Maurer, J., Materna, 2023. Quantification of geodetic strain rate uncertainties and implications for seismic hazard estimates. In: Geophysical Journal International. https://doi.org/10.1093/gji/ggad191.
McAlpin, David B., Meyer, Franz J., Gong, Wenyu, Beget, James E., Webley, Peter W., 2017. Pyroclastic flow deposits and InSAR: analysis of long-term subsidence at Augustine volcano, Alaska. Remote Sens. 9 (1), 2072–4292. https://doi.org/10.3390/rs9010004 issn. https://www.mdpi.com/2072-4292/9/1/4.
Melosh, Benjamin L., Rowe, Christie D., Gerbi, Christopher, Smit, Louis, Paul, Macey, 2018. Seismic cycle feedbacks in a mid-crustal shear zone. J. Struct. Geol. 112, 95–111. https://doi.org/10.1016/j.jsg.2018.04.004 issn: 0191-8141.
Mirzaee, S., Amelung, F., 2017. What InSAR time-series methods are best suited for the Ecuadorian volcanoes. AGU Fall Meeting Abstracts 2017 (G23A-0891), G23A–891.
Mirzaee, Sara, Amelung, Falk, Fattahi, Heresh, 2023. "Non-linear phase linking using joined distributed and persistent scatterers". en. Comput. Geosci. 171, 105291. https://doi.org/10.1016/j.cageo.2022.105291 issn: 00983004.
Mirzaee, Sara, Amelung, Falk, Mothes, Patricia, Yepez, Marco, 2021. Earthquake triggering of volcanic unrest in Ecuador at Guagua Pichincha and Chiles-Cerro Negro constrained by InSAR data. AGU Fall Meeting Abstracts 2021 (G24B-04). G24B–04.
Morales, A., Amelung, F., Mothes, P., Hong, Sang-Hoon, Nocquet, Jean-Mathieu, Paul, Jarrin, 2017. Ground deformation before the 2015 eruptions of Cotopaxi volcano detected by InSAR. Geophys. Res. Lett. 44 (13), 6607–6615. https://doi.org/10.1002/2017GL073720.
Morishita, Yu, Lazecky, Milan, Wright, Tim, Weiss, Jonathan, Elliott, John, Hooper, Andy, 2020. "LiCSBAS: An Open-Source InSAR Time Series Analysis Package Integrated with the LiCSAR Automated Sentinel-1 InSAR Processor". en. Remote Sens. 12 (3), 424. https://doi.org/10.3390/rs12030424 issn: 2072-4292.
Mothes, Patricia A., Jean-Mathieu, Nocquet, Paul, Jarrín, 2013. "Continuous GPS Network Operating Throughout Ecuador". en. Eos, Transactions American Geophysical Union 94 (26), 229–231. https://doi.org/10.1002/2013EO260002 issn: 0096-3941,2324-9250.
Mothes, Patricia A., Rolandone, Frederique, Nocquet, Jean-Mathieu, Jarrin, Paul A., Alvarado, Alexandra P., Ruiz, Mario C., Cisneros, David, Páez, Héctor Mora, Segovia, Mónica, 2018. "Monitoring the Earthquake Cycle in the Northern Andes from the Ecuadorian cGPS Network". en. Seismol Res. Lett. 89 (2A), 534–541. https://doi.org/10.1785/0220170243 issn: 0895-0695, 1938-2057.
Murphy, Benjamin, Müller, Sebastian, Yurchak, Roman, 2021. GeoStat-Framework/PyKrige: v1.6.1 (v1.6.1). url: Zenodo. https://doi.org/10.5281/zenodo.5380342.
Naranjo, M. Fernanda, Ebmeier, Susanna K., Vallejo, Silvia, Ramón, Patricio, Mothes, Patricia, Biggs, Juliet, Herrera, Francisco, 2016. "Mapping and measuring lava volumes from 2002 to 2009 at El Reventador Volcano, Ecuador, from field measurements and satellite remote sensing". en. Journal of Applied Volcanology 5 (1), 8. https://doi.org/10.1186/s13617-016-0048-z issn: 2191-5040.
Nocquet, J.-M., Villegas-Lanza, J.C., Chlieh, M., Mothes, P.A., Rolandone, F., Jarrin, P., Cisneros, D., Alvarado, A., Audin, L., Bondoux, F., Martin, X., Font, Y., Régnier, M., Vallée, M., Tran, T., Beauval, C., Maguiña Mendoza, J.M., Martinez, W., Tavera, H., Yepes, H., 2014. "Motion of continental slivers and creeping subduction in the northern Andes". en. Nat. Geosci. 7 (4), 287–291. https://doi.org/10.1038/ngeo2099 issn: 1752-0894, 1752-0908.
Nocquet, J.-M., Jarrin, P., Vallée, M., Mothes, P.A., Grandin, R., Rolandone, F., Delouis, B., Yepes, H., Font, Y., Fuentes, D., Régnier, M., Laurendeau, A., Cisneros, D., Hernandez, S., Sladen, A., Singaucho, J.-C., Mora, H., Gomez, J., Montes, L., Charvis, P., 2017. "Supercycle at the Ecuadorian subduction zone revealed after the 2016 Pedernales earthquake". en. Nat. Geosci. 10 (2), 145–149. https://doi.org/10.1038/ngeo2864 issn: 1752-0894, 1752-0908.
Ofeigsson, B.G., Hooper, A., Sigmundsson, F., Sturkell, E., Grapenthin, R., 2011. Deep magma storage at Hekla volcano, Iceland, revealed by InSAR time series analysis. J. Geophys. Res. Solid Earth 116, B05401. https://doi.org/10.1029/2010JB007576.
Ou, Q., Daout, S., Weiss, J.R., Shen, L., Lazecký, M., Wright, T.J., Parsons, B.E., 2022. "Large-Scale Interseismic Strain Mapping of the NE Tibetan Plateau From Sentinel-1 Interferometry". en. J. Geophys. Res. Solid Earth 127 (6), 2169–9356. https://doi.org/10.1029/2022JB024176 issn: 2169-9313.
Palin, Richard M., Santosh, M., 2021. "Plate tectonics: What, where, why, and when?" en. Gondwana Res. 100, 3–24. https://doi.org/10.1016/j.gr.2020.11.001 issn: 1342937X.
Parizzi, Alessandro, Brcic, Ramon, De Zan, Francesco, 2021. "InSAR Performance for Large-Scale Deformation Measurement". en. IEEE Trans. Geosci. Rem. Sens. 59 (10), 8510–8520. https://doi.org/10.1109/TGRS.2020.3039006 issn: 0196-2892, 1558-0644.
Pedersen, R., Sigmundsson, F., 2006. Temporal development of the 1999 intrusive episode in the Eyjafjallajökull volcano, Iceland, derived from InSAR images. Bull. Volcanol. 68, 377–393. https://doi.org/10.1007/s00445-005-0020-y.
Pedoja, Kevin, Ortlieb, Luc, Dumont, Jean-François, Lamothe, Michel, Ghaleb, Bassam, Marine, Auclair, Labrousse, Benoit, 2006. Quaternary coastal uplift along the Talara Arc (Ecuador, Northern Peru) from new marine terrace data. Mar. Geol. 228, 73–91. https://doi.org/10.1016/j.margeo.2006.02.014.
Pedoja, Kevin, François Dumont, Jean, Ortlieb, Luc, 2009. Levantamiento Cuaternario costero del Arco de Talara (Ecuador y norte del Perú): cuantificaciones con las secuencias de terrazas marinas. In: Geología y Geofísica marina y terrestre del Ecuador desde la costa continental hasta las islas Galápagos. Comisión Nacional del Derecho del Mar, Institut de Recherche pour le Développement and Instituto Oceanográfico de la Armada (INOCAR), pp. 107–129.
Pennington, Wayne D., 1981. Subduction of the eastern Panama basin and seismotectonics of northwestern South America. J. Geophys. Res. Solid Earth 86 (B11), 10753–10770. https://doi.org/10.1029/JB086iB11p10753.eprint.
Perfit, Michael R., Davidson, Jon P., Sigurdsson, H., 2000. Plate tectonics and volcanism. In: Encyclopedia of Volcanoes, pp. 89–113.
Poland, Michael P., Zebker, Howard A., 2022. Volcano geodesy using InSAR in 2020: the past and next decades. Bull. Volcanol. 84, 27. https://doi.org/10.1007/s00445-022-01531-1.
Pratt, Warren T., Duque, Pablo, Ponce, Miguel, 2005. An autochthonous geological model for the eastern Andes of Ecuador. Tectonophysics 399 (1–4), 251–278. https://doi.org/10.1016/j.tecto.2004.12.025 issn: 0040-1951.
Purcell, Victoria, Reddin, Eoin, Ebmeier, Susanna, González, Pablo J., Watson, Andrew, Morishita, Yu, Elliott, John, 2022. "Nearly Three Centuries of Lava Flow Subsidence at Timanfaya, Lanzarote". en. Geochem. Geophys. Geosystems 23 (10), 1525–2027. https://doi.org/10.1029/2022GC010576 issn: 1525-2027.
Python Software Foundation, 2022. Python 3.10.4. Accessed: Month Day, Year. url: https://www.python.org/.
Ramon, Patricio, Vallejo, Silvia, Mothes, Patricia, Andrade, Daniel, Vásconez, Francisco, Yepes, Hugo, Hidalgo, Silvana, Santamaría, Santiago, 2021. "Instituto Geofísico – Escuela Politécnica Nacional, the Ecuadorian Seismology and Volcanology Service". In: Volcanica 4.S1, pp. 93–112. https://doi.org/10.30909/vol.04.S1.93112 issn: 26103540.
Reyes, Pedro S.B., Ramírez, Milton R., Cajas, Marcelo I., 2020. "Detecting a master thrust system by magnetotelluric sounding along the western Andean Piedmont of Quito, Ecuador". en. Terra Nova 32 (6), 458–467. https://doi.org/10.1111/ter.12483 issn: 0954-4879, 1365-3121.
Richter, A., Ivins, E., Lange, H., Mendoza, L., Schröder, L., Hormaechea, J.L., Casassa, G., Marderwald, E., Fritsche, M., Perdomo, R., Horwath, M., Dietrich, R., 2016. "Crustal deformation across the Southern Patagonian Icefield observed by GNSS". en. Earth Planet Sci. Lett. 452, 206–215. https://doi.org/10.1016/j.epsl.2016.07.042 issn: 0012821X.
Rikitake, Tsuneji, 1976. "Recurrence of great earthquakes at subduction zones". en. Tectonophysics 35 (4), 335–362. https://doi.org/10.1016/0040-1951(76)90075-5 issn: 00401951.
Rolandone, Frederique, Nocquet, Jean-Mathieu, Mothes, Patricia A., Jarrin, Paul, Vallée, Martin, Cubas, Nadaya, Hernandez, Stephen, Plain, Morgan, Vaca, Sandro, Font, Yvonne, 2018. "Areas prone to slow slip events impede earthquake rupture propagation and promote afterslip". en. Sci. Adv. 4 (1), eaao6596. https://doi.org/10.1126/sciadv.aao6596 issn: 2375-2548.
Ruff, Larry J., 2013. "Large Earthquakes in Subduction Zones: Segment Interaction and Recurrence Times". en. In: Bebout, Gray E., Scholl, David W., Kirby, Stephen H., Platt, John P. (Eds.), Geophysical Monograph Series. American Geophysical Union, Washington, D. C., pp. 91–104. https://doi.org/10.1029/GM096p0091 isbn: 978-1-118-66457-5 978-0-87590-078-0.
Santamaria, Santiago, 2017. Catálogo de eventos volcánicos ocurridos en el Ecuador continental desde el Plioceno y análisis de la frecuencia eruptiva. Escuela Politécnica Nacional, Quito-Ecuador.
Savage, J.C., Burford, R.O., 1973. Geodetic determination of relative plate motion in central California. J. Geophys. Res. 78 (5), 832–845.
Schellart, W.P., 2007. "The potential influence of subduction zone polarity on overriding plate deformation, trench migration and slab dip angle". en. Tectonophysics 445 (3–4), 363–372. https://doi.org/10.1016/j.tecto.2007.09.009 issn: 00401951.
Scott, C., Bunds, M., Shirzaei, M., Toke, N., 2020. Creep along the central san Andreas Fault from surface fractures, topographic differencing, and InSAR. J. Geophys. Res. Solid Earth 125, e2020JB019762. https://doi.org/10.1029/2020JB019762.
Sierra, Daniel, 2015. "Determinación del estado de esfuerzos tectónicos en la zona del complejo volcánico Chiles-Cerro negro". es. PhD thesis. Escuela Politécnica Nacional, Quito-Ecuador.

Smith-Konter, Bridget R., Sandwell, David T., Shearer, Peter, 2011. "Locking depths estimated from geodesy and seismology along the San Andreas Fault System: Implications for seismic moment release". en. J. Geophys. Res. 116 (B6), B06401. https://doi.org/10.1029/2010JB008117 issn: 0148-0227.

Staller, Alejandra, álvarez-Gómez, José Antonio, Luna, Marco P., Béjar Pizarro, Marta, Gaspar-Escribano, Jorge M., Martínez-Cuevas, Sandra, 2018. Crustal motion and deformation in Ecuador from cGNSS time series. J. S. Am. Earth Sci. 86, 94–109. https://doi.org/10.1016/j.jsames.2018.05.014 issn: 0895-9811.

Stamps, D.S., Kreemer, C., 2024. Open access GNSS data for studies of the lithosphere. Geochem. Geophys. Geosystems 25, e2024GC011567. https://doi.org/10.1029/2024GC011567.

Stern, Robert J., 2002. "SUBDUCTION ZONES". en. Reviews of Geophysics 40.4. https://doi.org/10.1029/2001RG000108 issn: 8755-1209, 1944-9208.

Trenkamp, Robert, Kellogg, James N., Freymueller, Jeffrey T., Mora, Hector P., 2002. Wide plate margin deformation, southern Central America and northwestern South America, CASA GPS observations. J. S. Am. Earth Sci. 15 (2), 157–171. https://doi.org/10.1016/S0895-9811(02)00018-4.

Twardzik, Cedric, Vergnolle, Mathilde, Sladen, Anthony, Avallone, Antonio, 2019. "Unravelling the contribution of early postseismic deformation using sub-daily GNSS positioning". en. Sci. Rep. 9 (1), 1775. https://doi.org/10.1038/s41598-019-39038-z issn: 2045-2322.

Vaca, Sandro, Vallée, Martin, Nocquet, Jean-Mathieu, Alvarado, Alexandra, 2019. Active deformation in Ecuador enlightened by a new waveform-based catalog of earthquake focal mechanisms. J. S. Am. Earth Sci. 93, 449–461. https://doi.org/10.1016/j.jsames.2019.05.017 issn: 0895-9811.

Vasconez, Francisco J., Hidalgo, Silvana, Battaglia, Jean, Hernandez, Stephen, Benjamin, Bernard, Coppola, Diego, Valade, Sébastien, Ramón, Patricio, Arellano, Santiago, Liorzou, Céline, Almeida, Marco, Ortíz, Marcelo, Córdova, Jorge, Müller, Anais Vásconez, 2022. "Linking ground-based data and satellite monitoring to understand the last two decades of eruptive activity at Sangay volcano, Ecuador". en. Bull. Volcanol. 84 (5), 49. https://doi.org/10.1007/s00445-022-01560-w issn: 1432-0819.

Villegas-Lanza, J.C., Chlieh, M., Cavalié, O., Tavera, H., Baby, P., Chire-Chira, J., Nocquet, J.-M., 2016. "Active tectonics of Peru: Heterogeneous interseismic coupling along the Nazca megathrust, rigid motion of the Peruvian Sliver, and Subandean shortening accommodation: Active Tectonics of Peru". en. J. Geophys. Res. Solid Earth 121 (10), 7371–7394. https://doi.org/10.1002/2016JB013080 issn: 21699313.

Wang, Dehua, Elliott, John R., Zheng, Gang, Wright, Tim J., Watson, Andrew R., McGrath, Jack D., 2024. Deciphering interseismic strain accumulation and its termination on the central-eastern Altyn Tagh fault from high-resolution velocity fields. Earth Planet Sci. Lett. 644, 118919. https://doi.org/10.1016/j.epsl.2024.118919 issn: 0012-821X.

Watson, Andrew R., Elliott, John R., Walters, Richard J., 2022. "Interseismic Strain Accumulation Across the Main Recent Fault, SW Iran, From Sentinel-1 InSAR Observations". en. J. Geophys. Res. Solid Earth 127 (2), 2169–9356. https://doi.org/10.1029/2021JB022674 issn: 2169-9313.

Watson, A.R., Elliott, J.R., Lazecký, M., Maghsoudi, Y., McGrath, J.D., Walters, R.J., 2024. An InSAR-GNSS velocity field for Iran. Geophys. Res. Lett. 51, e2024GL108440. https://doi.org/10.1029/2024GL108440, 10.1029/2024GL108440.

Weiss, Jonathan R., Walters, Richard J., Morishita, Yu, Wright, Tim J., Lazecky, Milan, Wang, Hua, Hussain, Ekbal, Hooper, Andrew J., Elliott, John R., Rollins, Chris, Yu, Chen, González, Pablo J., Spaans, Karsten, Li, Zhenhong, Parsons, Barry, 2020. "High-Resolution Surface Velocities and Strain for Anatolia From Sentinel-1 InSAR and GNSS Data". en. Geophys. Res. Lett. 47 (17). https://doi.org/10.1029/2020GL087376 issn: 0094-8276, 1944-8007.

Werner, Charles, Wegmüller, Urs, Strozzi, Tazio, Wiesmann, Andreas, 2000. GAMMA SAR and interferometric processing software. Thunstrasse 130, CH-3074 Muri B. Bern, Switzerland: Gamma Remote Sensing.

Westerhoff, Rogier, Steyn-Ross, Moira, 2020. Explanation of InSAR Phase Disturbances by Seasonal Characteristics of Soil and Vegetation. en. Remote Sens. 12 (18), 3029. https://doi.org/10.3390/rs12183029 issn: 2072-4292.

Winter, T., Avouac, J.P., Lavenu, A., 1993. Late Quaternary kinematics of the Pallatanga strike-slip fault (central Ecuador) from topographic measurements of displaced morphological features. Geophys. J. Int. 3, 905–920.

Wright, T., Parsons, Barry E., Lu, Zhong, 2004. Toward mapping surface deformation in three dimensions using InSAR. Geophys. Res. Lett. https://doi.org/10.1029/2003GL018827.2004.

Wright, T.J., Houseman, G.A., Fang, J., Maghsoudi, Y., Hooper, A.J., Elliott, J.R., Evans, L., Lazecky, M., Ou, Q., Parsons, B.E., Rollins, J.C., Shen, L., Wang, H., 2023. High-resolution geodetic strain rate field reveals internal deformation of Tibetan Plateau. https://doi.org/10.31223/X5G95R.

Xu, Xiaohua, Sandwell, David T., Klein, Emilie, Bock, Yehuda, 2021. "Integrated Sentinel-1 InSAR and GNSS Time-Series Along the San Andreas Fault System". en. J. Geophys. Res. Solid Earth 126 (11), 2169–9356. https://doi.org/10.1029/2021JB022579 issn: 2169-9313.

Yepes, Hugo, Audin, Laurence, Alvarado, Alexandra, Beauval, Céline, Aguilar, Jorge, Font, Yvonne, Cotton, Fabrice, 2016. A new view for the geodynamics of Ecuador: implication in seismogenic source definition and seismic hazard assessment: Ecuador GEODYNAMICS AND PSHA. Tectonics 35 (5), 1249–1279. https://doi.org/10.1002/2015TC003941.

Yepez, M., Trasatti, E., Tolomei, C., Atzori, S., Mothes, P., Ruiz, M., Samaniego, P., 2020. "InSAR Deformation Analysis and Source Modelling of the Guagua Pichincha Volcano (Ecuador)". en. In: IGARSS 2020 - 2020 IEEE International Geoscience and Remote Sensing Symposium. IEEE, Waikoloa, HI, USA, pp. 6854–6856. https://doi.org/10.1109/IGARSS39084.2020.9324031 isbn: 978-1-72816-374-1.

Yepez, Marco, Mothes, Patricia, Trasatti, Elisa, Tolomei, Cristiano, Atsori, Simone, 2021. InSAR Monitoring of Ground Deformation at the Chiles – Cerro Negro Volcanic Complex (Ecuador).

Yu, Chen, Li, Zhenhong, Penna, Nigel T., Crippa, Paola, 2018. "Generic Atmospheric Correction Model for Interferometric Synthetic Aperture Radar Observations". en. J. Geophys. Res. Solid Earth 123 (10), 9202–9222. https://doi.org/10.1029/2017JB015305 issn: 2169-9313, 2169-9356.

Zhao, Dapeng, Qu, Cheng, Bürgmann, Roland, Gong, Wei, Shan, Xinjian, Qiao, Xuejun, et al., 2022a. Large-scale crustal deformation, slip-rate variation, and strain distribution along the Kunlun Fault (Tibet) from Sentinel-1 InSAR observations (2015–2020). J. Geophys. Res. Solid Earth 127 (9), e2021JB022892. https://doi.org/10.1029/2021JB022892.

Zhao, Dezheng, Qu, Chunyan, Bürgmann, Roland, Gong, Wenyu, Shan, Xinjian, Qiao, Xin, Zhao, Lei, Chen, Han, Liu, Lian, 2022b. Large-scale crustal deformation, slip-rate variation, and strain distribution along the Kunlun fault (Tibet) from Sentinel-1 InSAR observations (2015–2020). J. Geophys. Res.

Weiss, Jonathan R., Qiang Qiu, Sylvain Barbot, Tim J. Wright, James H. Foster, Alexander Saunders, Benjamin A. Brooks, Michael Bevis, Eric Kendrick, Todd L. Ericksen, Jonathan Avery, Robert Smalley, Sergio R. Cimbaro, Luis E. Lenzano, Jorge Barón, Juan Carlos Báez, and Arturo, Echalar (2019). "Illuminating subduction zone rheological properties in the wake of a giant earthquake". en. In: Science Advances 5.12, eaax6720. issn: 2375-2548. doi: 10.1126/sciadv.aax6720.

Cando Jácome, M., Martinez-Graña, A.M., and Valdés, V, 2020. Detection of Terrain Deformations Using InSAR Techniques in Relation to Results on Terrain Subsidence (Ciudad de Zaruma, Ecuador). In: Remote Sensing 12.10, p. 1598. issn: 2072-4292. doi: 10.3390/ rs12101598. https://www.mdpi.com/2072-4292/12/10/1598.

Instituto Geofísico (IG-EPN), 2022, Informe Especial del volcán Chiles – Cerro Negro No. 3. Tech. rep. 1. Instituto Ge- ofisico IG-EPN. https://www.igepn.edu.ec/servicios/noticias/1946-informe- especial-complejo-volcanico-chiles-cerro-negro-no-2022-03.